

The [C II] line emission as an ISM probe in the MARIGOLD galaxies

Prachi Khatri, Emilio Romano-Díaz, and Cristiano Porciani

Argelander Institute für Astronomie, Auf dem Hügel 71, D-53121 Bonn, Germany
e-mail: pkhatri@astro.uni-bonn.de

Received / Accepted

ABSTRACT

Context. The [C II] fine-structure line at $157.74 \mu\text{m}$ is one of the brightest far-infrared emission lines in galaxies and an important probe of galaxy properties such as the star formation rate (SFR) and the molecular gas mass (M_{mol}).

Aims. Using high-resolution numerical simulations, we test the reliability of the [C II] line as a tracer of M_{mol} in high-redshift galaxies and investigate secondary dependencies of the [C II] – M_{mol} relation on the SFR and metallicity. We also investigate the time evolution of the [C II] luminosity function (LF) and the relative spatial extent of [C II] emission and star formation.

Methods. We post-process galaxies from the MARIGOLD cosmological simulations at redshifts $3 \leq z \leq 7$ to obtain their [C II] emission. These simulations were performed with the sub-grid chemistry model, HYACINTH, to track the non-equilibrium abundances of H_2 , CO, C and C^+ on the fly. Based on a statistical sample of galaxies at these redshifts, we investigate correlations between the [C II] line luminosity ($L_{[\text{C II}]}$) and the SFR, the M_{mol} , the total gas mass and the metal mass in gas phase (M_{metal}).

Results. We find that accounting for secondary dependencies in the $L_{[\text{C II}]} - M_{\text{mol}}$ relation improves the M_{mol} prediction by a factor of 2.3 at all redshifts. Our simulations predict a mild evolution in the slope of the $L_{[\text{C II}]} - \text{SFR}$ relation ($\lesssim 0.15$ dex) and an increase in the intercept by 0.5 dex in the above redshift range. Among the various galaxy properties we explore, the [C II] emission in our simulated galaxies shows the tightest correlation with M_{metal} , indicating the potential of this line to constrain the metallicity of high-redshift galaxies. About 20% (10%) of our simulated galaxies at $z = 5$ ($z = 4$) have [C II] emission extending ≥ 2 times farther than the star formation activity. The [C II] LF evolves rapidly and is always well approximated by a double power law that does not show an exponential cutoff at the bright end. We record a 600-fold increase in the number density of $L_{[\text{C II}]} \sim 10^9 L_{\odot}$ emitters in 1.4 Gyr.

Key words. methods: numerical – galaxies: high-redshift – galaxies: formation – galaxies: emission

1. Introduction

The fine-structure line of singly-ionised carbon (C^+) at a wavelength of $157.74 \mu\text{m}$ (hereafter [C II]), is an important coolant in the interstellar medium (ISM) of galaxies near and far. Being one of the brightest lines in the infrared, accounting for $\sim 0.1 - 1\%$ of the total infrared luminosity in star-forming galaxies (Díaz-Santos et al. 2013), it is particularly useful for observing high-redshift ($z \gtrsim 4$) galaxies, where it is conveniently redshifted to the transparent atmospheric window at millimetre wavelengths and is accessible from the ground with the Atacama Large Millimeter/submillimeter Array (ALMA) and Northern Extended Millimeter Array (NOEMA), among others.

The strength of this line has been shown to correlate well with both the galaxy-integrated star formation rate (SFR; Stacey et al. 2010; De Looze et al. 2011, 2014; Carniani et al. 2018; Matthee et al. 2019; Schaerer et al. 2020) and the spatially-resolved SFR (the $\Sigma_{[\text{C II}]} - \Sigma_{\text{SFR}}$ relation; Pineda et al. 2014; De Looze et al. 2014; Herrera-Camus et al. 2015). Additionally, in recent years, the line strength has been used as a tracer of other galaxy-integrated quantities such as the molecular gas mass (Hughes et al. 2017; Madden et al. 2020; Zanella et al. 2018), particularly of CO-dark molecular gas (Madden et al. 2020; Accurso et al. 2017), the H I mass (Heintz et al. 2021, 2022), the total gas mass (D'Eugenio et al. 2023), as well as the metal content (Heintz et al. 2023). However, it is known from observations of [C II] emission from galactic centres and luminous infrared galaxies, with infrared (IR) luminosities $L_{\text{IR}} \gtrsim 10^{11} L_{\odot}$, that the $L_{[\text{C II}]} / L_{\text{IR}}$ ratio decreases with increasing L_{IR} (e.g., Mal-

hotra et al. 2001; Graciá-Carpio et al. 2011; Díaz-Santos et al. 2013), thereby hinting at a possible breakdown of the [C II]-SFR relation at high SFRs or high SFR surface densities (see e.g., Graciá-Carpio et al. 2011).

From the theoretical point of view, the observed correlations between [C II] line strength and the galaxy properties arise naturally as [C II] is a metal cooling line and is linked to both the metal content and the heating via star formation in regions where cooling is dominated by this line such as photon-dominated regions (PDRs) and the cold neutral medium. Moreover, the various galaxy properties are themselves correlated; for example, the Kennicutt-Schmidt relation connects the gas surface density and the SFR surface density (Kennicutt 1998; Leroy et al. 2008; Bigiel et al. 2008), while the mass-metallicity relation (Tremonti et al. 2004) connects the stellar mass and gas metallicity. This implies that any correlation of the [C II] line with another galaxy property will have secondary dependencies, often manifested as a scatter, that must be quantified to provide robust calibrations.

In this regard, the [C II]-SFR correlation has garnered a lot of attention on the theoretical front. Several studies have meticulously tested this correlation and its redshift evolution using chemical and radiative transfer modelling in individual galaxies (Vallini et al. 2015; Katz et al. 2019, 2022) or for entire simulation suite at targeted redshifts (Olsen et al. 2016, 2017; Pallottini et al. 2017; Lagache et al. 2018; Lupi et al. 2018; Popping et al. 2019; Leung et al. 2020).

However, unlike the [C II]-SFR relation, the [C II] – M_{mol} relation has received limited attention in simulations so far (see e.g., Vizgan et al. 2022), partly because current state-of-the-

arXiv:2411.09755v1 [astro-ph.GA] 14 Nov 2024

art cosmological simulations do not self-consistently follow the evolution of the molecular gas component in galaxies, and they often rely on analytical relations to be used in post-processing (e.g., [Lagos et al. 2015, 2016](#)), which might not hold at high redshifts. For instance, [Vizgan et al. \(2022\)](#) found a shallower $L_{[\text{C II}]} - M_{\text{mol}}$ relation at $z \sim 6$ compared to the one obtained by [Zanella et al. \(2018\)](#) using a compilation of $M_* \gtrsim 10^{10} M_{\odot}$ galaxies at $z = 0 - 5.5$, highlighting the need for robust testing of this calibration.

Therefore, while observations of the $[\text{C II}]$ line have opened up an interesting avenue for probing the high- z ISM, several open questions still remain: does the $[\text{C II}]$ -SFR relation evolve with redshift? Does the $[\text{C II}]$ - M_{mol} relation show secondary dependencies on other galaxy properties? What is faint-end slope of the $[\text{C II}]$ luminosity function and how does it evolve with redshift? To provide a theoretical insight on these, we have performed a suite of cosmological simulations, called the MARIGOLD suite, wherein we follow the non-equilibrium abundance of H_2 , CO, C, and C^+ on the fly using the sub-grid model HYACINTH ([Khatri et al. 2024](#)). The $[\text{C II}]$ emission from the simulated galaxies is calculated by solving the radiative-transfer problem in post-processing. In this paper, we use this simulation suite to investigate the usefulness of this line as a probe of the interstellar medium (ISM) in high-redshift ($3 \leq z \leq 7$) galaxies. In particular, we provide a calibration for inferring the molecular gas mass of a galaxy from its $[\text{C II}]$ luminosity, accounting for secondary dependencies in this relation across redshift.

In the past few years, observations of high-redshift galaxies have detected $[\text{C II}]$ emission extending farther than the UV continuum emission from these galaxies ([Fujimoto et al. 2019, 2020](#); [Ginolfi et al. 2020](#); [Fudamoto et al. 2022](#); [Lambert et al. 2023](#); [Posses et al. 2024](#)), hinting at an extended gas reservoir rich in ionized carbon. This extended $[\text{C II}]$ emission is often referred to as a $[\text{C II}]$ halo, despite the misleading term. Satellites galaxies, galactic outflows, and gas stripped due to galaxy interactions are all plausible sources of an extended $[\text{C II}]$ halo. Reproducing extended $[\text{C II}]$ in numerical simulations has proven challenging so far ([Fujimoto et al. 2019](#); [Muñoz-Elgueta et al. 2024](#)), making it difficult to pinpoint its exact origin(s). This is further complicated by the faint nature of the extended emission and the limited spatial resolution of high- z observations. In this study, we further explore the existence of extended $[\text{C II}]$ emission using our simulations.

The rest of the paper is organised as follows: In Sect. 2, we describe the simulation suite and detail the modelling of the $[\text{C II}]$ emission in Sect. 3. In Sect. 4, we investigate the redshift evolution of the $[\text{C II}]$ luminosity function from the simulations. We investigate the $[\text{C II}]$ -star formation rate correlation in our simulated galaxies on global and spatially resolved scales in Sect. 5. In Sect. 6, we examine the reliability of the $[\text{C II}]$ line as a molecular gas tracer and quantify secondary dependencies of the $L_{[\text{C II}]} - M_{\text{mol}}$ relation on the star formation rate and the gas metallicity. Then, we explore the extended $[\text{C II}]$ emission in Sect. 7. We compare our $[\text{C II}]$ -SFR relation and $[\text{C II}]$ luminosity function with those from previous numerical studies in Sect. 8 and conclude with a summary of our main results in Sect. 9.

2. Simulations

We use the MARIGOLD suite of cosmological simulations ([Khatri et al., in preparation](#)), which comprises two hydrodynamical simulations – a $(25 \text{ Mpc})^3$ comoving volume (M25) and a $(50 \text{ Mpc})^3$ comoving volume (M50). The simulations and the statistical properties of the simulated galaxies are described in full detail in

[Khatri et al. \(to be submitted\)](#). Here we briefly summarize some key details.

The simulations adopt the Planck cosmology ([Planck Collaboration VI 2020](#)) with $\Omega_{\Lambda} = 0.6847$, $\Omega_{\text{m}} = 0.3153$, $\Omega_{\text{b}} = 0.0493$, $\sigma_8 = 0.8111$, $n_s = 0.9649$, and $h = 0.6736$. The simulations are started from uni-grid initial conditions (ICs) set at $z = 99$ generated with the code MUSIC ([Hahn & Abel 2011](#)). The ICs have an initial refinement level $l_{\text{initial}} = 10$ corresponding to 1024^3 grid cells and an equal number of dark matter particles. We allow the grid to refine naturally down to $z = 3$, which results in a maximal spatial resolution (i.e., minimum grid cell size Δx^{min} in physical units) achieved during the course of the simulations of $\Delta x^{\text{min}} = 32 \text{ pc}$ for M25 and $\Delta x^{\text{min}} = 64 \text{ pc}$ for M50. The simulation volumes have periodic boundary conditions and the dynamical evolution of dark matter, gas, and stars is tracked with the adaptive mesh refinement code RAMSES ([Teysier 2002](#)) down to $z = 3$. The simulation specification are given in Table 1.

These simulations were performed using the sub-grid model HYACINTH ([Khatri et al. 2024](#)) to evolve the non-equilibrium abundances of H_2 , CO, C, and C^+ . HYACINTH comprises a sub-grid chemical network based on our modified version of the widely used [Nelson & Langer \(1999\)](#) chemical network. It accounts for the unresolved density structure of the ISM by assuming a probability distribution function (PDF) of sub-grid densities. The PDF is designed to vary with the state of star formation. A metallicity-dependent temperature-density relation based on high-resolution molecular cloud simulations ([Hu et al. 2021](#)) assigns a (sub-grid) temperature to each sub-grid density. The chemical rate equations are solved at each sub-grid density and the cell-averaged chemical abundances are obtained by integrating over the density PDF. The model is described in full detail in [Khatri et al. \(2024\)](#).

We use the Amiga Halo Finder [Knollmann & Knebe \(AHF 2009\)](#) to identify halos and subhalos in each snapshot. AHF identifies halos by locating density peaks within the simulation and then iteratively determining the gravitationally bound particles that constitute each peak. Each resulting halo is a spherical region with virial radius R_{vir} and a mean matter density (i.e., including dark matter, gas, and stars) equal to 200 times the critical density ρ_{crit} . The virial mass of the halo can be written as $M_{\text{vir}} = \frac{4}{3}\pi R_{\text{vir}}^3 200 \rho_{\text{crit}}$, where the masses and sizes of haloes are calculated accounting for unbinding. These are referred to as ‘main halos’ in the following. Subhalos are defined as gravitationally bound objects within main halos and lying within common isodensity contours of the host halo. We impose that every halo is resolved with at least a 100 particles, unless otherwise specified (see e.g., Sect. 4). Galaxies are defined in terms of their parent halo. For main haloes, the stellar concentration at their centre is referred to as the main galaxy. For each main galaxy, we start with a spherical region of size $0.1 R_{\text{vir}}$ and calculate the stellar half-mass radius $r_{1/2,*}$ (that is, the radius containing half of the stellar mass within $0.1 R_{\text{vir}}$). The galaxy is defined in terms of $2r_{1/2,*}$ and all (galaxy-integrated) quantities are measured within this radius. Conversely, the stellar concentration residing at the centre of a subhalo is called a satellite galaxy whose size is defined by the radius corresponding to the maximum of the subhalo rotation curve, $R_{V_{\text{max}}}$ ([Klypin et al. 2011](#); [Prada et al. 2012](#)). In other words, $R_{V_{\text{max}}}$ sets the boundary of a satellite galaxy. To ensure that the stellar component of the galaxies is well resolved, we impose a cut of 100 stellar particles (which results in different stellar mass cuts for the two simulations). Our M25 simulation is capable of resolving low-mass galaxies down to a stellar mass of $10^6 M_{\odot}$, while our M50 run is aimed at improving the statis-

Table 1: Specifications of the MARIGOLD simulation suite. From left to right, the columns list: the name of the simulation, the comoving box size, the number of dark-matter (DM) particles, the initial and final refinement levels, the minimum cell size achieved in the simulation in physical units, the DM and stellar particle masses, and the average gas mass per grid cell in the initial conditions.

Simulation	L_{box} (cMpc)	N_{DM}	l_{initial}	l_{final}	Δx^{min} (pc)	m_{DM} (M_{\odot})	m_{*} (M_{\odot})	$m_{\text{gas}}^{\text{ini}}$ (M_{\odot})
M25	25	1024^3	10	17	32	5.0×10^5	7.2×10^3	9.3×10^4
M50	50	1024^3	10	17	64	4.0×10^6	5.8×10^4	7.4×10^5

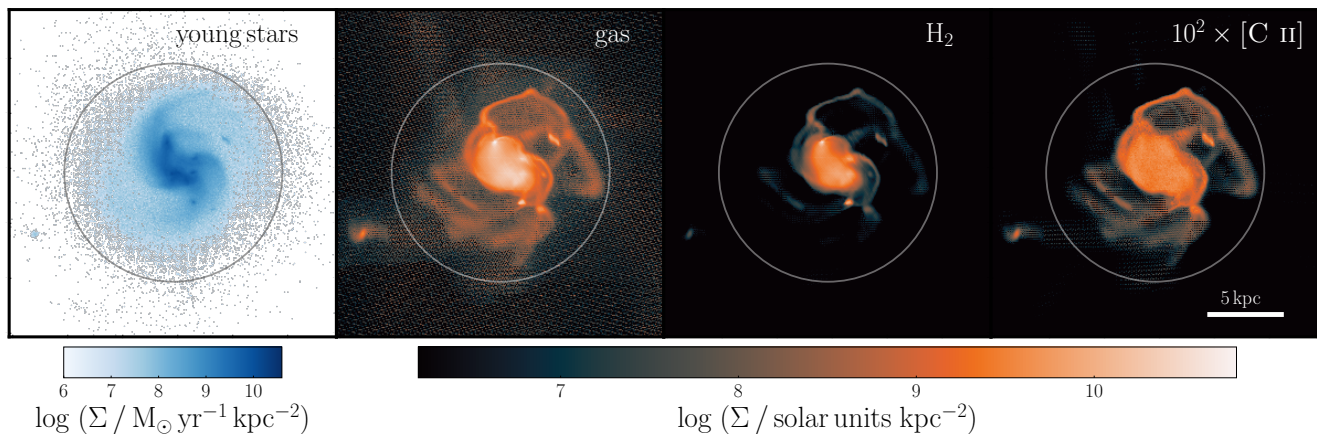


Fig. 1: Face-on view of a simulated galaxy at $z = 4$. From left to right, the columns show the surface density of young stars (with ages ≤ 200 Myr), total gas surface density, H_2 surface density, and [C II] surface brightness. In each panel the circle indicates 0.1 times the virial radius of the parent DM halo.

tical robustness of our results and its larger volume allows us to simulate more massive galaxies.

3. Modelling [C II] emission

The first ionization potential of atomic carbon (11.3 eV) is lower than that of hydrogen (13.6 eV). Consequently, singly-ionized carbon (C^+) exists in different ISM phases including molecular clouds, neutral atomic gas, and H II regions and emits the [C II] fine-structure line in a variety of conditions. Disentangling the contribution of the different phases to the total [C II] emission of a galaxy is therefore challenging and requires using other emission lines.

Observational studies of [C II] emission in $z \gtrsim 1$ galaxies have shown that the bulk of the [C II] emission originates from PDRs that represent a transition region between the H II region around a young massive star and a molecular cloud. For instance, Stacey et al. (2010) found that in a sample of 12 galaxies at $1 \lesssim z \lesssim 2$, more than 70% of the [C II] emission arises from PDRs. Also, Gullberg et al. (2015) found that in their sample of 20 dusty star-forming galaxies at $2.1 < z < 5.7$, the [C II] emission is consistent with arising from PDRs. This finding is further supported by theoretical studies that calculate the [C II] emission from simulated galaxies in post-processing, accounting for emission arising from different phases, e.g., Olsen et al. (2015), who employ a multi-phase ISM model for each gas particle in the simulation and use the photoionisation code CLOUDY (Ferland et al. 1992) to calculate the emission arising from each phase (also see Pallottini et al. 2017). The general consensus from these studies is that the bulk ($\gtrsim 70 - 90\%$) of the [C II] emission arises from neutral atomic and molecular gas. Moreover, based on a sample of low-metallicity dwarf galaxies from the *Herschel* Dwarf Galaxy Survey (Madden et al. 2013), Cormier et al. (2019) found that

$\gtrsim 70\%$ [C II] emission arises from PDRs. As such galaxies are expected to be similar to high-redshift galaxies in terms of their ISM structure, it is reasonable to assume that a similar fraction of the [C II] emission arises from PDRs in high-redshift galaxies as well.

We use HYACINTH to obtain the abundances of H_2 , CO, C, and C^+ in our simulations. HYACINTH follows a simplified chemical network and predicts abundances that are consistent with PDR codes (Wolfire et al. 2010). This approach allows us to model the [C II] emission without relying on assumptions regarding the C^+ abundance that might not hold across the entire galaxy population at all redshifts.

The [C II] line arises from the $^2P_{3/2} \rightarrow ^2P_{1/2}$ fine-structure transition of C^+ , that can be excited by collisions with hydrogen molecules (H_2), hydrogen atoms (H), and electrons (e^-). The transition can also be excited by an external radiation field such as the cosmic microwave background (CMB), which becomes particularly important at higher redshifts (da Cunha et al. 2013). De-excitation can either happen spontaneously or be stimulated by the external radiation field.

When calculating the [C II] emission from a simulated galaxy, we account for optical depth effects within individual cells. For this we assume a plane-parallel configuration and divide each cell into N slices. The density in each slice is obtained from the underlying density PDF (same as in HYACINTH; see also Vallini et al. 2015). The level populations in each slice are computed accounting for the emission from all other slices. Conversely, the fraction of emission from a given slice that manages to reach the edge of the cell (where the optical depth $\tau = 0$) depends on the slice's position within the cell depends on its location within the cell. Solving this radiative transfer problem requires an iterative approach, which is detailed in Appendix A. We validate our model against CLOUDY in Appendix B.

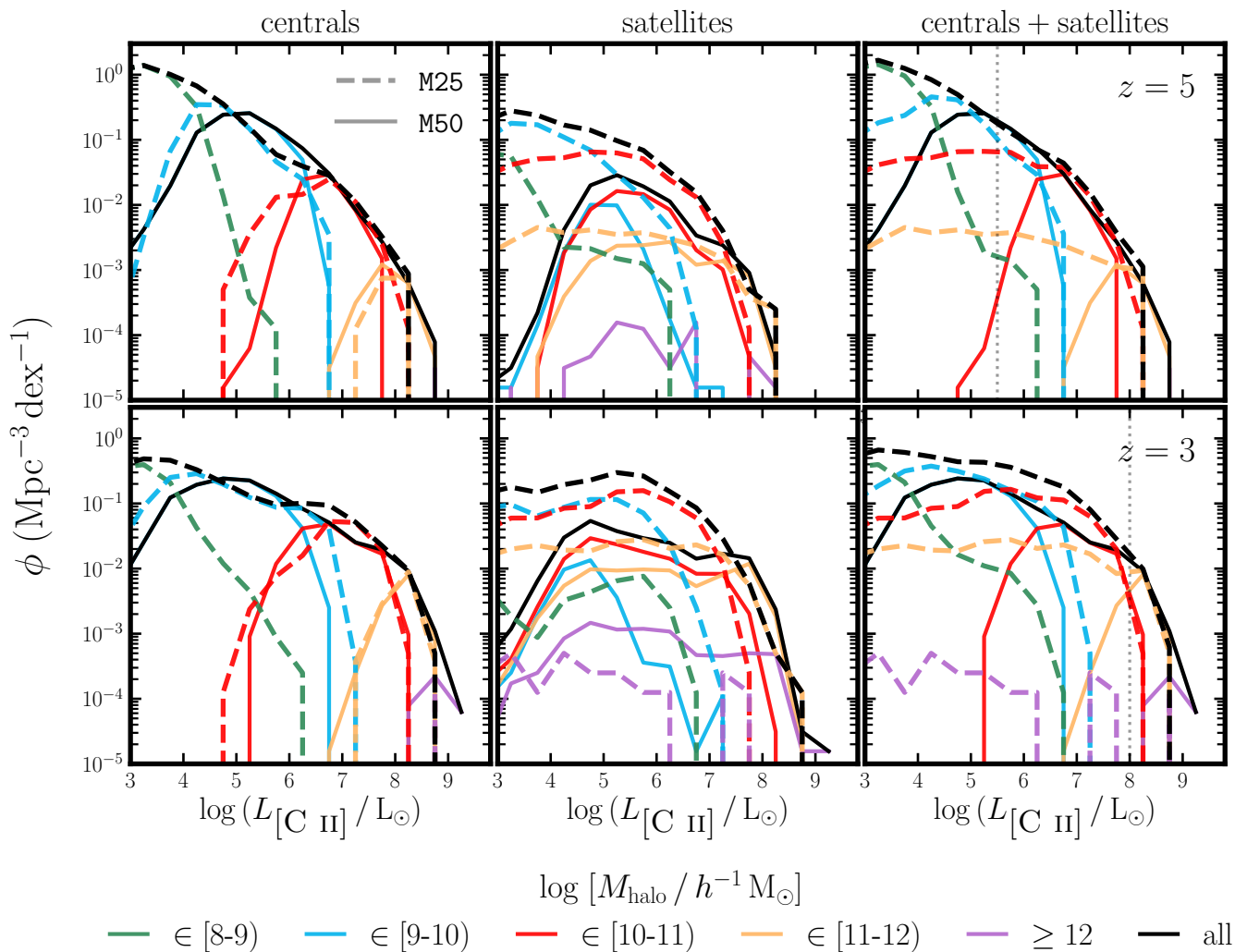


Fig. 2: Conditional [C II] LF from the M25 (dashed lines) and M50 (solid lines) simulations at redshifts $z = 5$ and 3 for central galaxies (left panels), satellites galaxies (middle panels), and all galaxies (right panels). The coloured lines show the CLF of emitters residing in DM halos in different M_{halo} bins and the black lines show the total LFs. The dotted grey line in the right panels denotes the luminosity threshold, L_{thr} , below which the total LFs from two simulations differ significantly due to resolution effects.

However, when calculating the total [C II] luminosity of a galaxy, we assume that the cells are radiatively decoupled from each other. This means that the [C II] emission that escapes the cell of origin, travels unattenuated to the edge of the galaxy. This assumption is valid whenever the velocity difference between neighbouring cells is larger than the intrinsic line width due to the gas motions within a cell: the emitted spectra is shifted out of the frequency range where it could be absorbed by another cell. This is a common approximation in the literature (see e.g. Olsen et al. 2015; Vallini et al. 2015). The total [C II] luminosity of the galaxy is then calculated as the sum of the luminosities of each cell within the galaxy.

Fig. 1 shows the different baryonic components and the [C II] surface brightness of a simulated galaxy at $z = 4$.

4. [C II] luminosity function

In this section, we examine the [C II] luminosity function (LF) from the MARIGOLD simulations and investigate how it evolves with redshift.

4.1. Conditional luminosity function and resolution effects

The difficulty we have to face is to combine simulations with different spatial and mass resolutions in a consistent way while accounting for sample variance given the relatively small computational volumes. For these reasons, we first perform a consistency check between the outputs of M25 and M50 by measuring the conditional luminosity function (CLF, Yang et al. 2003), i.e. the luminosity function of emitters hosted by DM halos within a narrow mass bin. We only consider (main) halos containing more than 300 DM particles and examine three different cases: (i) central galaxies only, (ii) satellite galaxies only, and (iii) centrals+satellites. Our results for $z = 5$ and 3 are shown in Fig. 2. These cases are representative of what happens in the redshift ranges $5 \leq z \leq 7$ and $3 \leq z < 5$, respectively.

For all halo masses, the CLFs of the central galaxies in the two simulations are in excellent agreement. The CLF has a characteristic bell shape and its width grows with decreasing halo mass. Conversely, satellites have a much broader CLF and M25 presents many more faint satellites than M50 at fixed halo mass. This dis-

crepancy reflects the different mass and spatial resolutions in the simulations that regulate the abundance of DM satellites and the [C II] emission from their gas, respectively. Inspection of the total LF reveals that the two simulations show small differences (which are compatible with sample variance) above a threshold luminosity L_{thr} and substantial systematic differences for $L_{[\text{C II}]} < L_{\text{thr}}$. We find that $L_{\text{thr}} \approx 10^{5.5} L_{\odot}$ for $5 \leq z \leq 7$ and $L_{\text{thr}} \approx 10^8 L_{\odot}$ for $3 \leq z < 5$ (dotted grey lines in the right panels of Fig. 2). This confirms that, as we stated before, our high-resolution M25 simulation is excellent for probing the faint end of the LF while the M50 simulation is ideally suited for probing the bright end because of its larger volume.

Finally, we note that at $L_{[\text{C II}]} \geq 10^5 L_{\odot}$, the total luminosity function is fully represented by halos with masses $M_{\text{halo}} \geq 10^9 h^{-1} M_{\odot}$. Therefore, in the following, we restrict our analysis to these ranges of luminosities and masses.

4.2. Bayesian curve fitting

At each redshift, we fit the simulated LF, $\phi(L_{[\text{C II}]}) = dn/d \log L_{[\text{C II}]}$ ¹, with different functional forms. Based on the discussion above, we consider all galaxies with $L_{[\text{C II}]} \geq 10^5 L_{\odot}$ hosted by halos with $M_{\text{halo}} \geq 10^9 h^{-1} M_{\odot}$ from M25 but only those with $L_{[\text{C II}]} > L_{\text{thr}}$ from M50. For the functional forms, we consider a Schechter function,

$$\phi(L_{[\text{C II}]}) = \ln(10) \phi_* \left(\frac{L_{[\text{C II}]}}{L_*} \right)^{\alpha+1} \exp\left(-\frac{L_{[\text{C II}]}}{L_*}\right), \quad (1)$$

and a double power-law (DPL),

$$\phi(L_{[\text{C II}]}) = \ln(10) \phi_* \left[\left(\frac{L_{[\text{C II}]}}{L_*} \right)^{-(\alpha+1)} + \left(\frac{L_{[\text{C II}]}}{L_*} \right)^{-(\beta+1)} \right]^{-1}. \quad (2)$$

where all parameters have the usual meaning and $\beta < \alpha$.

We follow a Bayesian approach and sample the parameter space using a Markov-chain Monte-Carlo (MCMC) method implemented with the python package *emcee* (Foreman-Mackey et al. 2013). We assume that the counts N_i in each logarithmic bin of luminosity follow a Poisson distribution and write the log-likelihood function for each simulation as

$$\ln \mathcal{L} = \sum_{i=1}^{N_{\text{bins}}} N_i \ln(N_{\text{model},i}) - N_{\text{model},i} + \text{constant}. \quad (3)$$

Eventually, we sum the results obtained for M25 and M50.

To account for the sample variance of the simulated volumes, we follow an approach that builds upon the method originally proposed by Trenti & Stiavelli (2008) to obtain the LF from the combination of observational data with different depths. Briefly, we fit the LF data from the two simulations with exactly the same shape but (slightly) different normalisation factors that can be written as $\log \phi_{*,j} = \log \phi_* + \Delta_j$, where ϕ_* represents the ‘cosmic’ normalization and Δ_j is the correction due to sample variance in the j^{th} simulation. We impose independent Gaussian priors on each Δ_j , i.e., $\Delta_j \sim \mathcal{N}(0, (\sigma_{v,j}/\ln 10)^2)$, where $\sigma_{v,j}^2$ is the sample variance of the overdensity within the respective simulation volume. The latter is estimated from the calculations presented in Somerville et al. (2004), considering the halo mass

¹ Note that here and throughout the text, we use ‘log’ to denote \log_{10} ; for the natural logarithm \log_e , we use ‘ln’ instead.

bin that gives the dominant contribution to the counts of emitters around L_* . We adopt (broad) flat priors on all other parameters.

As an example, we show in Appendix C, the resulting posterior distribution for the DPL fit at $z = 3$. In what follows, we present results obtained after marginalising the posterior distributions over the parameters, Δ_j .

Since computing the model evidence from the Markov chains is problematic, for simplicity, we use the deviance information criterion (DIC, Spiegelhalter et al. 2002) to identify whether the Schechter function or the DPL provide a better fit to the simulated data. Deviance is a measure of goodness of fit defined as $D = -2 \ln \mathcal{L}(\theta)$, where θ indicates the parameters of a model. The DIC is obtained correcting the deviance with a penalty, p_{D} , for the complexity of the model which is quantified in terms of the effective number of fit parameters. There are two common approaches to estimate p_{D} from a Markov chain: $p_{\text{D}}^{(a)} = \overline{D(\theta)} - D(\bar{\theta})$ and $p_{\text{D}}^{(b)} = \text{Var}(D)/2$, where an overbar denotes the average over the posterior distribution (i.e. over the sampled chain) and the symbol Var denotes the corresponding variance. The DIC is then defined as $\text{DIC} = D(\bar{\theta}) + 2p_{\text{D}}$. Models with smaller DIC are better supported by the data. Typically, differences (ΔDIC) above 5 are considered substantial and the model with the higher DIC is ruled out if the difference grows above 10. Based on this test, we find that the LF from our simulations is better represented by a DPL. The corresponding parameters are listed in Table 2 along with the ΔDIC values computed with both estimators for p_{D} . We provide in Appendix C a comparison of the two functional forms with the simulation data.

Fig. 3 shows the resulting [C II] luminosity function obtained using a DPL at different redshifts. The shaded band indicates the central 68% credibility region obtained with the MCMC method. The solid line represents the best fit (evaluated at the posterior mean $\bar{\theta}$). We see a clear redshift evolution in the LF. The turnover luminosity (L_*) increases (almost) monotonically with time and the faint-end slope (α) tends to flatten at late times. In contrast, the bright-end slope (β) does not show a clear evolutionary trend. The large jump in the LF at $L_{[\text{C II}]} \lesssim 10^8 L_{\odot}$ is partially due to the spatial refinement that happens shortly after $z = 5$ in both simulations, that allows them, especially M25, to resolve more emitters. We also see a significant evolution in the number density of bright emitters. The number density of galaxies at $L_{[\text{C II}]} \sim 10^9 L_{\odot}$ increases from $\sim 10^{-6} \text{ dex}^{-1} \text{ Mpc}^{-3}$ at $z = 7$ to $6 \times 10^{-4} \text{ dex}^{-1} \text{ Mpc}^{-3}$ at $z = 3$, indicating a 600-fold increase in the number of $L_{[\text{C II}]} \sim 10^9 L_{\odot}$ galaxies in a less than 1.5 Gyr timespan.

Observational constraints on the [C II] luminosity function at these redshifts come from Yan et al. (2020) for targeted detections at $4.5 \lesssim z \lesssim 5.9$ in the ALMA Large Program to Investigate C⁺ at Early Times² (ALPINE Le Fèvre et al. 2020) and a lower limit at $z \sim 4.4$ reported by Swinbank et al. (2012) based on [C II] detections in two observed galaxies. We find that our LFs at $z = 5$ and 4 are in excellent agreement with both estimates. We compare against previous numerical work in Sect. 8.

4.3. [C II] luminosity density

Measuring the cosmic star formation rate density (SFRD) at different epochs has been the subject of several studies (see Madau & Dickinson 2014, for a complete review). Similarly, estimating the cosmic molecular gas density from blind and targeted surveys of molecular gas tracers such as CO and dust continuum

² <http://alpine.ipac.caltech.edu/>

Table 2: Best-fit parameters to the LF for the DPL function given in Eq. (2). The last two columns show the values of ΔDIC^a and ΔDIC^b between the Schechter function and the DPL (see text).

z	$\log(\phi_* / \text{Mpc}^{-3} \text{dex}^{-1})$	$\log(L_* / L_\odot)$	α	β	$\Delta\text{DIC}^{(a)}$	$\Delta\text{DIC}^{(b)}$
7	$-1.84^{+0.15}_{-0.15}$	$6.44^{+0.10}_{-0.11}$	$-1.54^{+0.06}_{-0.05}$	$-2.75^{+0.08}_{-0.09}$	105	107
6	$-1.26^{+0.12}_{-0.12}$	$6.20^{+0.10}_{-0.10}$	$-1.24^{+0.06}_{-0.06}$	$-2.30^{+0.04}_{-0.05}$	222	223
5	$-1.52^{+0.13}_{-0.13}$	$6.72^{+0.11}_{-0.11}$	$-1.42^{+0.03}_{-0.03}$	$-2.31^{+0.05}_{-0.05}$	159	161
4	$-0.91^{+0.08}_{-0.07}$	$7.03^{+0.04}_{-0.04}$	$-1.28^{+0.01}_{-0.01}$	$-2.57^{+0.05}_{-0.05}$	449	451
3	$-1.00^{+0.08}_{-0.08}$	$7.37^{+0.04}_{-0.04}$	$-1.22^{+0.01}_{-0.01}$	$-2.65^{+0.05}_{-0.05}$	174	176

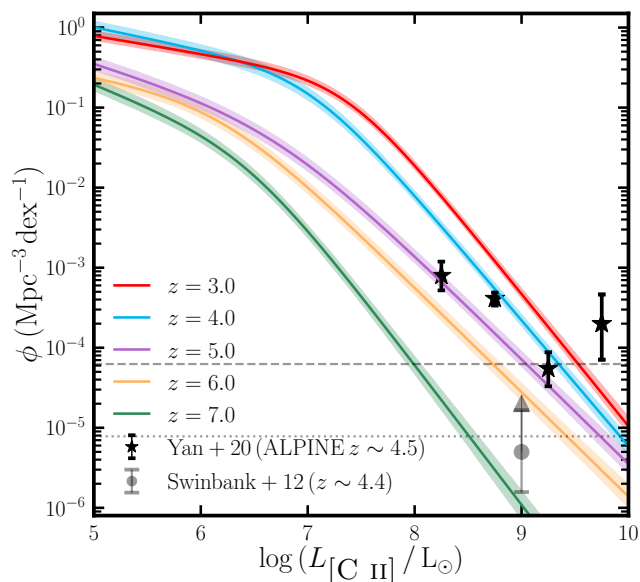


Fig. 3: The simulated $[\text{C II}]$ LF compared with observational estimates. The coloured lines represent the best-fit DPL – Eq. (2) – to the simulated LF and the shaded area represents the central 68% credibility range obtained using the MCMC chains. Black stars represent the observational estimates at $z \sim 4.5$ from the ALPINE survey (Yan et al. 2020) and the grey arrow shows the lower limit from Swinbank et al. (2012) based on observations of two galaxies at $z \sim 4.4$. The dashed and dotted horizontal lines represent a number count of 1 per dex in the entire simulation volume of M25 and M50, respectively.

(see e.g. Walter et al. 2020; Riechers et al. 2019; Scoville et al. 2017; Magnelli et al. 2020, among others) has also gained significant interest over the last decade. Owing to the correlation between the $[\text{C II}]$ luminosity with both the SFR and molecular gas mass across redshift, estimates of the cosmic $[\text{C II}]$ luminosity density ($\rho_{[\text{C II}]}$) can be used to infer the cosmic SFRD and the cosmic molecular gas density (see e.g., Yan et al. 2020; Loiacono et al. 2021 for the ALPINE survey and Aravena et al. 2024 for the Reionization Era Bright Emission Line Survey³, REBELS, Bouwens et al. 2022).

In Fig. 4, we show the redshift evolution of $\rho_{[\text{C II}]}$ predicted by our simulations and compare with observational estimates at these redshifts. For this we integrate the LF in Fig. 3 down to $\log(L_{\text{min}} / L_\odot) = 5$. This is shown by a black line in Fig. 4 and referred to as our fiducial estimate in the following. For a fair comparison with observational estimates of $\rho_{[\text{C II}]}$ from

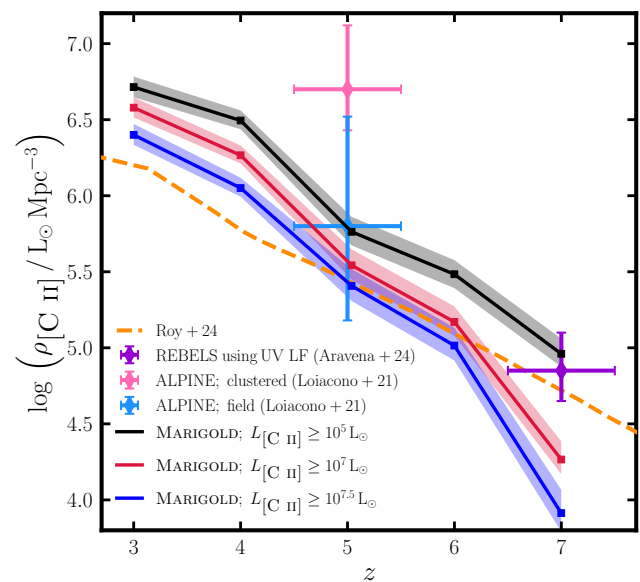


Fig. 4: Comparison of the cosmic $[\text{C II}]$ luminosity density ($\rho_{[\text{C II}]}$) for different luminosity cuts in the MARIGOLD simulations with observational estimates from ALPINE (Loiacono et al. 2021) – clustered and field estimates in pink and blue, respectively; from REBELS (Aravena et al. 2024) in purple and from a semi-empirical model by Roy & Lapi (2024) shown as an orange dashed line. The $\rho_{[\text{C II}]}$ from the simulations is obtained by integrating the LFs shown in Fig. 3 down to $\log(L_{\text{min}} / L_\odot) = 5$ (black), 7 (red), and 7.5 (blue). The shaded regions represent the 16-84 percentile range of $\rho_{[\text{C II}]}$ obtained from the LFs.

the ALPINE (Loiacono et al. 2021) and REBELS (Aravena et al. 2024) surveys, we show using red and blue lines, respectively, the $\rho_{[\text{C II}]}$ (z) for $\log(L_{\text{min}} / L_\odot) = 7$ and $\log(L_{\text{min}} / L_\odot) = 7.5$, which correspond to the luminosity cuts adopted in the two surveys for integrating the luminosity function. Note that Loiacono et al. (2021) provide two estimates for $\rho_{[\text{C II}]}$ based on serendipitously detected galaxies in ALPINE at $z \sim 5$; one of these is obtained by integrating the $[\text{C II}]$ LF based on a sample of galaxies that seem to be part of a local overdensity and are therefore not representative of the galaxy population at the targeted redshift (this is referred to as the ‘clustered estimate’). The $\rho_{[\text{C II}]}$ for the field population (the ‘field estimate’) can be estimated by only considering emitters detected outside the aforementioned overdensity. Since there is only such emitter detected in their sample, Loiacono et al. (2021) obtain the field estimate by multiplying the clustered estimate by the ratio between the number of emitters in the field and clustered subsamples (=1/11), on account of the similar volumes estimated for the two subsamples. We find that the $\rho_{[\text{C II}]}$ predicted by our

³ <https://rebelsalma.wordpress.com/>

simulations at $z = 5$ shows an excellent agreement with that from ALPINE for their field sample, irrespective of the luminosity cut. Conversely, as expected, the $\rho_{[\text{C II}]}^{\text{clustered}}$ from ALPINE is almost an order of magnitude higher than our predicted $\rho_{[\text{C II}]}$. Our $\rho_{[\text{C II}]}$ at $z = 7$ is lower than the REBELS one when considering their luminosity cut of $10^{7.5} L_{\odot}$ (blue line), but our $\rho_{[\text{C II}]}$ with lower luminosity cuts (red and black lines) bracket the REBELS estimate. Overall, our estimates show a good agreement with observations. At $z \lesssim 4$, the impact of a luminosity cut is not as severe and alters the predicted $\rho_{[\text{C II}]}$ by at most a factor of 2.

We also include in Fig. 4, the $\rho_{[\text{C II}]}(z)$ estimate from Roy & Lapi (2024), based on a semi-empirical model that performs an abundance matching of the theoretical halo mass function and the observed stellar mass function, and assigns a [C II] luminosity to every halo based on the empirical SFR-stellar-mass relation and the [C II]-SFR relation from Vallini et al. (2015). The resulting $\rho_{[\text{C II}]}(z)$ from their approach is similar in shape to our fiducial estimate but consistently lower by a factor of ~ 2 in the redshift range shown here.

5. The $L_{[\text{C II}]} - \text{SFR}$ relation

We now turn our attention to investigating how the [C II] luminosity correlates with the SFR (this section) and the molecular gas mass (Sect. 6) using a statistical sample of simulated galaxies. For this, we only consider central galaxies as the [C II] LFs of the centrals from the two simulations show an excellent agreement across redshift (see the left panels of Fig. 2).

The luminosity of the [C II] line correlates strongly with the SFR in normal star-forming galaxies (Stacey et al. 2010; De Looze et al. 2014). It is one of the brightest emission lines in high- z galaxies and is unaffected by dust obscuration. Thus, it can provide an estimate of the total (unobscured+obscured) SFR in distant galaxies. Moreover, if the [C II]-SFR calibration does not evolve significantly with redshift, then it can be robustly used across cosmic time. In this section, we aim to investigate the correlation between [C II] luminosity ($L_{[\text{C II}]}$) and the SFR in the MARIGOLD galaxies on both galaxy-wide (Sects. 5.1- 5.2) and spatially-resolved (Sect. 5.3) scales.

5.1. Galaxy-integrated [C II]-SFR relation

Fig. 5 shows our simulated galaxies in the $L_{[\text{C II}]} - \text{SFR}$ plane for different redshifts. We calculate the SFR averaged over the last 200 Myr to be consistent with observations that commonly use a combination of SF tracers to estimate the total obscured + unobscured SF (see e.g. Kennicutt & Evans 2012; De Looze et al. 2014; Herrera-Camus et al. 2015; Lomaeva et al. 2022). For comparison, we show the best-fit relation from (De Looze et al. 2014) for their high-redshift sample ($0.5 \leq z \leq 6.6$, orange solid line). We further compare with [C II]-detected galaxies at $4.4 \leq z \leq 5.9$ from the ALPINE survey (B  thermin et al. 2020). The best-fit $L_{[\text{C II}]} - \text{SFR}$ for these galaxies (Schaerer et al. 2020) is shown using a blue solid line. We also include a literature sample of [C II]-detected galaxies compiled by Olsen et al. (2015) (pink symbols) and the galaxy REBELS-25 (black diamond Rowland et al. 2024) observed as part of REBELS. Many of our galaxies occupy the same region in the [C II]-SFR plane as the observed galaxies (shown as blue, pink, and black scatter points).

At each redshift, we fit a relation of the form $\log(L_{[\text{C II}]} / L_{\odot}) = a \log(\text{SFR}_{200} / M_{\odot} \text{ yr}^{-1}) + b$ (where $\{a, b\} \in \mathbb{R}^2$) to our simulated galaxies using an ordinary least squares linear regression (shown as a solid red line in Fig. 5). We report in Table 3 the re-

sulting parameters along with the 1σ dispersion, i.e., the standard deviation of the residuals around the best fit in each case.

Firstly, from the distribution of simulated galaxies at different redshifts in the [C II]-SFR plane, we immediately see an increase in $L_{[\text{C II}]}$ at a given SFR from $z = 7$ to $z = 3$, which is likely fueled by the buildup of the metal content of galaxies over time. We quantify this redshift evolution in Sect. 5.2. At $z = 3$, our galaxies are well-distributed around the De Looze et al. (2014) relation and our best fit is in excellent agreement with theirs, while at $z = 4$, we obtain a similar relation as Schaeerer et al. (2020) (considering conservative upper limits on [C II] non-detections to the ALPINE galaxy sample). The value of the Spearman's rank correlation coefficient, indicated in each panel in Fig. 5, increases with time and remains high (≥ 0.86) at all redshifts. We further find that the scatter $L_{[\text{C II}]} - \text{SFR}$ relation increases with increasing redshift, similar to previous findings by Carniani et al. (2018) for a sample of ~ 50 galaxies at $5 \lesssim z \lesssim 7$. In contrast, based on a semi-analytical galaxy formation model coupled to the spectral synthesis code CLOUDY (Ferland et al. 1992), Lagache et al. (2018) reported a slight decrease in the scatter of the $L_{[\text{C II}]} - \text{SFR}$ relation with redshift.

The [C II]-SFR connection on galaxy-wide scales has been investigated in previous numerical studies. We compare with these in Sect. 8.

5.2. Redshift evolution of the [C II] - SFR relation

An important question concerning the [C II]-SFR relation is whether it shows any evolution with redshift. For instance based on the ALPINE survey, Schaeerer et al. (2020) found that star-forming galaxies at $4 \lesssim z \lesssim 6$ follow the same or a slightly steeper [C II]-SFR relation compared to local galaxies (De Looze et al. 2014, shown as an orange line in Fig. 5), depending on the treatment of non-detections in their galaxy sample. For the MARIGOLD galaxies, the slope of the $L_{[\text{C II}]} - \text{SFR}$ relation shows little redshift evolution in the range $3 \leq z \leq 7$ ($\lesssim 0.15$ dex variation). As noted before, the best fit for our lowest redshift galaxy sample ($z = 3$) is in excellent agreement with the De Looze et al. (2014), but deviations towards lower $L_{[\text{C II}]}$ are evident at $z \gtrsim 5$. Consequently, at a given SFR, $L_{[\text{C II}]}$ decreases with increasing redshift. This trend can be attributed to the lower metallicity of galaxies at higher redshifts. For reference, the median metallicity of our galaxy sample, expressed as $12 + \log(\text{O}/\text{H})$ increases from 7.4 ± 0.2 at $z = 7$ to 7.9 ± 0.3 at $z = 3$ (the errors on the median metallicities denote the interquartile range). Similarly, for galaxies with $\log(\text{SFR} / M_{\odot} \text{ yr}^{-1}) = 1.0 \pm 0.25$, the median metallicity increases by ≈ 0.4 dex in this redshift range. The same is also reflected in the monotonically increasing values of the intercept b from $z = 7$ to $z = 3$ (see Table 3), which increases by a factor of ~ 3 (0.5 dex) in this redshift range. To conclude, we find a redshift evolution in the intercept of the [C II]-SFR relation, as evident from the offset between our best-fit relation and the De Looze et al. (2014) relation that is the same in all panels.

5.3. Spatially resolved [C II] - SFR relation

Resolved observations of [C II] and SF in high-redshift galaxies have found that these galaxies exhibit a “[C II] deficit” with respect to the local $\Sigma_{[\text{C II}]} - \Sigma_{\text{SFR}}$ relation. For example, Carniani et al. (2018) found that the galaxy-integrated [C II]-SFR relation at $5 \lesssim z \lesssim 7$ is similar to the local one but in the $\Sigma_{[\text{C II}]} - \Sigma_{\text{SFR}}$ plane, the galaxies have a substantially lower $\Sigma_{[\text{C II}]}$ compared to the local galaxies at any given Σ_{SFR} . They attributed the offset

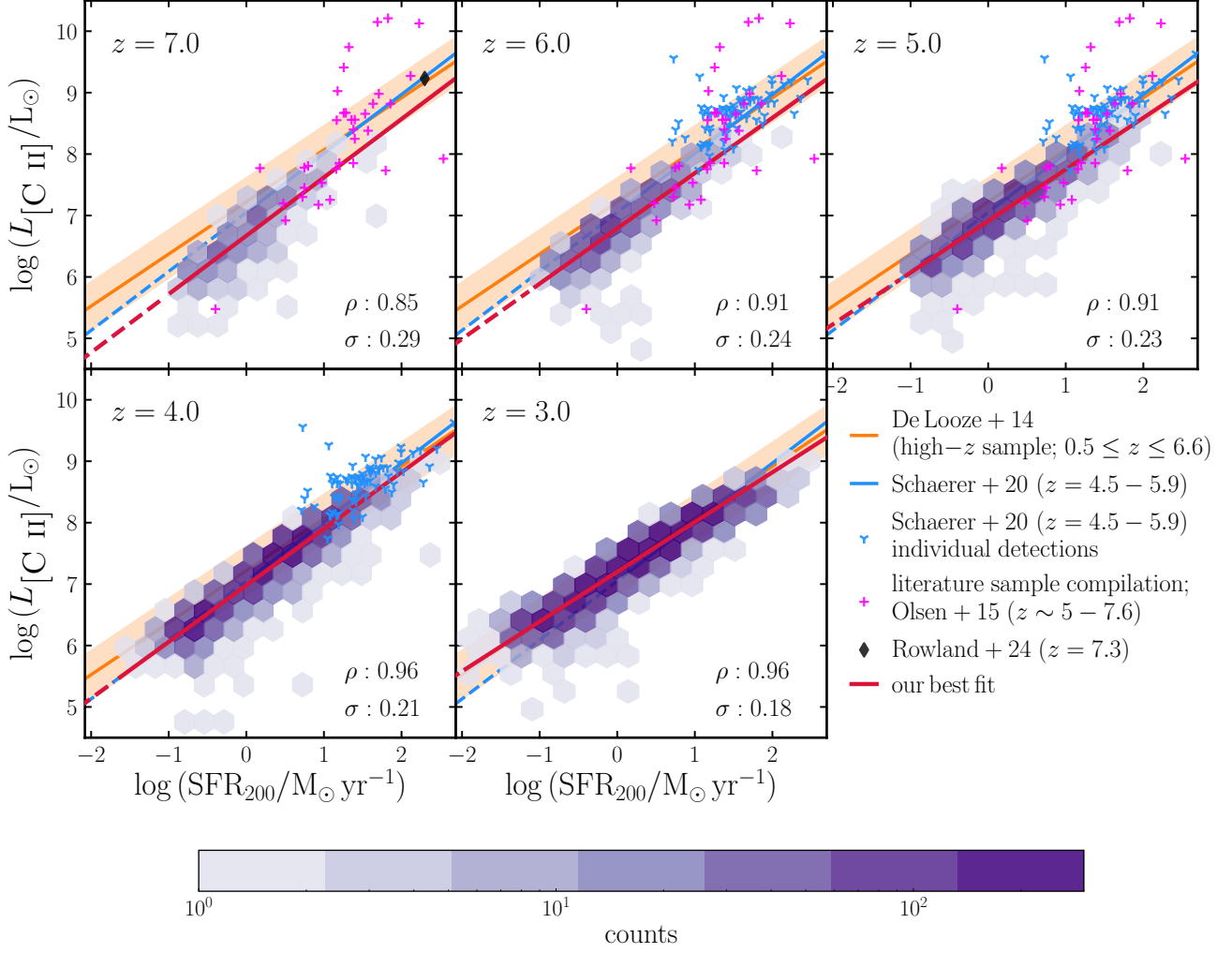


Fig. 5: The $[\text{C II}] - \text{SFR}$ relation from the MARIGOLD simulations at $3 \leq z \leq 7$ compared with observations. The simulated galaxy population is represented as purple hexbins, with the colour indicating the galaxy counts per bin. The red line showing the best-fit to these galaxies (see Table 3 for the fit parameters). In each panel, we report the Spearman's rank correlation coefficient (ρ) and the 1σ scatter around the best-fit relation. The best-fit relation from De Looze et al. (2014) for their high- z ($0.5 < z < 6.6$) sample is shown in orange, with the shaded area representing the 1σ scatter. The blue line indicates the best-fit relation for $4.5 \leq z \leq 5.9$ galaxies from the ALPINE survey (Schaefer et al. 2020). The best-fits mentioned above are extrapolated beyond the range constrained by the respective studies using a dashed line of the same colour. The individual ALPINE galaxies (at $4.5 \leq z \leq 5.9$), the literature sample (at $5 \leq z \leq 7.6$) taken from Olsen et al. (2015), and REBELS-25 from the REBELS survey Rowland et al. (2024) are shown with blue, pink, and black symbols, respectively.

mainly to the lower metallicity of these galaxies and stressed that the more extended $[\text{C II}]$ emission in high- z galaxies could also play a role.

Here we examine the (spatially-resolved) $\Sigma_{[\text{C II}]} - \Sigma_{\text{SFR}}$ relation in our simulated galaxies. For simplification, we present results based on $z = 4$ galaxies, although, qualitatively similar results are obtained for other redshifts as well. In each galaxy, the $[\text{C II}]$ surface brightness and SFR surface density are obtained from a face-on projection of a cube centred on the galaxy and of side length equal to twice the size of the galaxy. The spatial resolution (minimum grid cell size; see Table 1) of our simulations is better than that achieved in current high- z $[\text{C II}]$ observations that can resolve kpc-scale regions within $z \geq 4$ galaxies (e.g., Posses et al. 2024). Therefore, we apply a 2D Gaussian smoothing to our simulated surface brightness and surface density maps

to mimic observations. For this analysis, we adopt the beam sizes (in terms of the full-width at half-maximum, FWHM) for the SFR surface density and the $[\text{C II}]$ surface brightness measurements from Posses et al. (2024), which are $0.2''$ and $0.17''$, respectively. At $z = 4$, these correspond to ~ 1.4 kpc and ~ 1.2 kpc.

In the left panel of Fig. 6, we show the $\Sigma_{[\text{C II}]} - \Sigma_{\text{SFR}}$ relation for our simulated galaxies. We split our simulated galaxies into three groups according to their stellar mass (M_*), with the number of galaxies in each group indicated in the legend. For each group, solid lines show the median $\Sigma_{[\text{C II}]}$ as a function of Σ_{SFR} and the shaded area represents the interquartile range. The median $\Sigma_{[\text{C II}]}$ shows slight variations among the different M_* bins. Most notably, towards higher Σ_{SFR} , lower M_* galaxies exhibit a lower $\Sigma_{[\text{C II}]}$, likely because of their (relatively) lower metallicity. The median $\Sigma_{[\text{C II}]}$ in all M_* bins is lower than the local relation and

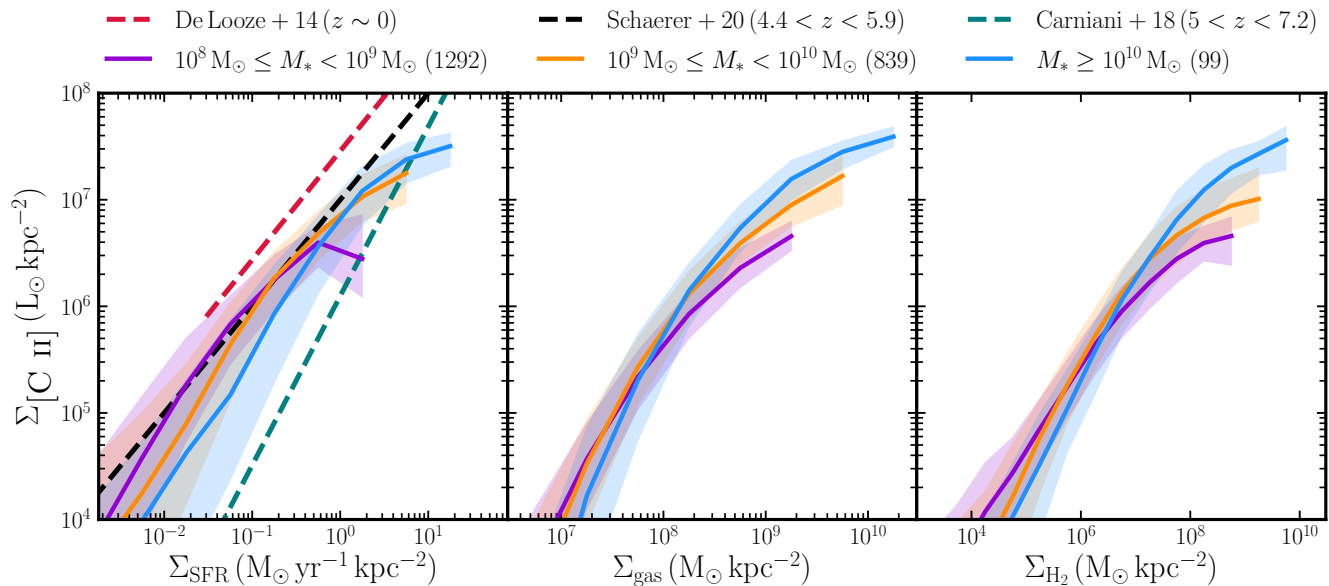


Fig. 6: The spatially-resolved [C II] – SFR relation for the MARIGOLD galaxies at $z = 4$. The galaxies are divided into different stellar-mass bins (the number of galaxies in each bin is indicated in the legend). The solid lines show the median $\Sigma_{[\text{C II}]}$ as a function of the SFR surface density (*left*), of the the gas surface density (*middle*), and of the H_2 surface density (*right*). The shaded areas represent the 16-84 percentile range. In the left panel, dashed lines indicate the empirical relations from De Looze et al. (2014, red) based on local dwarf galaxies from the *Herschel* Dwarf Galaxy Survey, for ALPINE galaxies in black (based on global values only Schaefer et al. 2020, black), and for a sample of galaxies at $5 < z < 7.2$ from Carniani et al. (2018, teal). For the simulated galaxies, the [C II] surface brightness, and the SFR, gas, and H_2 surface densities are obtained from a face-on projection of a cube centred on the galaxy and of side length equal to twice the radius of the galaxy.

similar to the relation from Schaefer et al. (2020, same as in Figure 12 of Posses et al. 2024). At $\Sigma_{\text{SFR}} \lesssim 1 \text{ M}_\odot \text{ yr}^{-1} \text{ kpc}^{-2}$, our medians for all M_* bins are consistent with the Schaefer et al. (2020) relation, but at higher Σ_{SFR} , they start to deviate towards lower $\Sigma_{[\text{C II}]}$ values and the shaded area overlaps with the Carniani et al. (2018). This trend continues towards higher Σ_{SFR} , and for $\Sigma_{\text{SFR}} \gtrsim 10 \text{ M}_\odot \text{ yr}^{-1} \text{ kpc}^{-2}$, the median $\Sigma_{[\text{C II}]}$ from our simulations is lower than the Schaefer et al. (2020) and Carniani et al. (2018) relations by a factor of ≈ 2.5 .

For the same galaxies, we also show the $\Sigma_{[\text{C II}]} - \Sigma_{\text{gas}}$ and $\Sigma_{[\text{C II}]} - \Sigma_{\text{H}_2}$ in Fig. 6. The gas surface densities are smoothed with a Gaussian beam of FWHM of $\sim 1.0 \text{ kpc}$ (same as for $\Sigma_{[\text{C II}]}$). Once again, there are no strong variations among the different M_* bins except at the highest gas surface densities. In the $\Sigma_{[\text{C II}]} - \Sigma_{\text{H}_2}$ plane, a similar trend is observed although with larger differences, similar to those in the $\Sigma_{[\text{C II}]} - \Sigma_{\text{SFR}}$ plane. We also observe that in all panels, the slope decreases towards higher surface densities.

5.3.1. Possible [C II]-deficit?

At $\Sigma_{\text{SFR}} \gtrsim 1 \text{ M}_\odot \text{ yr}^{-1} \text{ kpc}^{-2}$, our $\Sigma_{[\text{C II}]} - \Sigma_{\text{SFR}}$ relation deviates from the Schaefer et al. (2020) relation towards lower $\Sigma_{[\text{C II}]}$ and exhibit values similar to the Carniani et al. (2018) relation, albeit with a shallower slope. As regions of high SF are expected to be rich in dust and thereby bright in FIR emission, this trend is similar to the observed ‘[C II]-deficit’ i.e., the decrease in the ratio of the [C II] to the FIR luminosity in luminous infrared galaxies.

We investigate the underlying cause of this deficit by examining the surface density of C^+ , and CO as a function of Σ_{SFR} , Σ_{gas} ,

and the surface density of metals (Σ_{metals}) in our galaxies in Appendix D. We see that Σ_{C^+} plateaus towards high Σ_{SFR} and Σ_{gas} , while Σ_{CO} continues to grow. Firstly, a Σ_{gas} leads to a higher H_2 abundance. Second, a higher Σ_{SFR} is associated with a higher dust abundance; together these provide better shielding of CO against the dissociating UV radiation in dense environments. Therefore, in regions with a high SFR surface density, the bulk of the carbon is locked up in CO, leading to a flattening of Σ_{C^+} towards high Σ_{SFR} , and consequently a slower increase of the [C II] surface brightness towards high SFR and gas surface densities. Further note that our simulations do not account for the UV radiation from active galactic nuclei (AGN), that can contribute to the first ionization of carbon (and subsequently to [C II] emission). While some studies suggest that AGN are not a significant source of [C II] emission (see e.g., De Breuck et al. 2022), their contribution has not yet been estimated using a large sample of galaxies at high redshifts. However, the harder ionizing radiation from AGN can also ionize C^+ , resulting in a decrease in the [C II] emission (Langer & Pineda 2015). In this case, the [C II] luminosity could be even lower than predicted by our model.

A similar decline in [C II] was also reported by De Looze et al. (2014) (see their Figure 2) who found that the slope of the $\Sigma_{\text{SFR}} - \Sigma_{[\text{C II}]}$ relation steepens for $\Sigma_{[\text{C II}]} \gtrsim$ few times $10^6 \text{ L}_\odot \text{ kpc}^{-2}$ indicating that the [C II] line is not the dominant coolant in intensely star-forming regions. Such a deficit would manifest as a shallower slope of the $\Sigma_{[\text{C II}]} - \Sigma_{\text{SFR}}$ relation towards higher $\Sigma_{[\text{C II}]}$ (and higher Σ_{SFR}).

Overall we find that for our simulated galaxies at $z = 4$, the median $\Sigma_{[\text{C II}]}$ in a given Σ_{SFR} bin shows an excellent agreement with the best-fit to ALPINE galaxies at $4.4 \leq z \leq 5.9$ for $\Sigma_{\text{SFR}} \lesssim 1 \text{ M}_\odot \text{ yr}^{-1} \text{ kpc}^{-2}$. Towards higher Σ_{SFR} , however, the

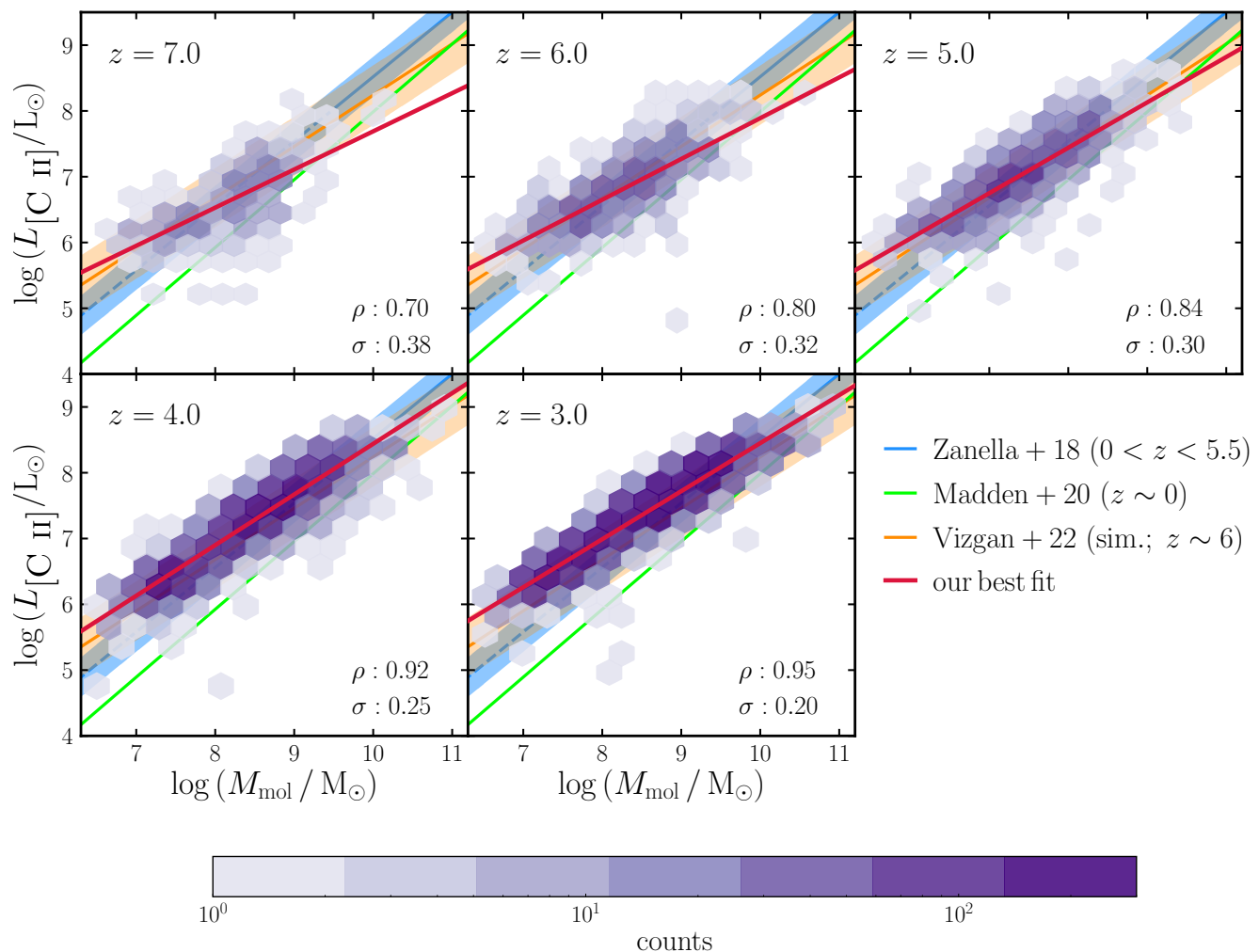


Fig. 7: The $[\text{C II}] - M_{\text{mol}}$ relation from our simulations compared with observations. The simulated galaxies are represented by purple hexbins, where the colour indicates the number of galaxies in each bin. The solid red line gives the ordinary least squares linear fit to these galaxies, with the fit parameters listed in Table 3. In each panel, we report the Spearman’s rank correlation coefficient (ρ) and the 1σ scatter around the best-fit relation. The best fit to the observed galaxy sample at $z = 0 - 5.5$ by Zanella et al. (2018) is shown in blue and the fit to the $z \sim 0$ dwarf galaxies (Madden et al. 2020) is shown in lime. The relation from SIMBA simulations at $z = 6$ (Vizgan et al. 2022) is shown in orange. As in Fig. 5, the extrapolated Zanella et al. (2018) relation is shown as a dashed line of the same colour.

median shows a flattening. This is driven by the increased abundance of CO at the expense of C^+ along high surface density lines of sight.

6. $[\text{C II}]$ emission as a molecular gas tracer

Zanella et al. (2018) identified a strong correlation between the luminosity of the $[\text{C II}]$ line and the molecular gas mass based on a compilation of galaxies in the redshift range $0 \leq z \leq 5.5$. Their sample includes local dwarf galaxies, main-sequence galaxies at $0 \leq z \leq 5.5$, starburst galaxies at $0 \lesssim z \lesssim 2$ and local luminous/ultra-luminous infrared galaxies. The best fit to their galaxy sample is given by:

$$\log \left(\frac{L_{[\text{C II}]}}{L_{\odot}} \right) = -1.28(\pm 0.21) + 0.98(\pm 0.02) \log \left(\frac{M_{\text{mol}}}{M_{\odot}} \right), \quad (4)$$

with a scatter of ≈ 0.3 dex around the best fit. Consequently, $[\text{C II}]$ emission is now routinely used as a molecular gas tracer in

high-redshift galaxies and it seems to be as good as conventional tracers like CO rotational lines and dust continuum emission. For instance, Dessauges-Zavadsky et al. (2020) found that the $[\text{C II}]$ -based molecular gas mass estimates for ALPINE galaxies were consistent with those derived from dynamical mass estimates and (rest-frame) infrared luminosities. Aravena et al. (2024) found similar results for REBELS galaxies at $6.5 \lesssim z \lesssim 7.5$.

However, this relation and its redshift evolution have not been extensively explored in numerical simulations. While Vizgan et al. (2022) investigated the $[\text{C II}] - M_{\text{mol}}$ relation in SIMBA simulations at a specific redshift of $z \sim 6$, a detailed study at different epochs is still lacking. To address this, here we examine the $[\text{C II}]$ -molecular gas connection in the MARIGOLD galaxies at different redshifts and develop a prescription for inferring the molecular gas mass of a galaxy from its $[\text{C II}]$ emission. In Fig. 7, we compare the $L_{[\text{C II}]} - M_{\text{mol}}$ relation for our simulated galaxies at different redshifts against the calibrations from Zanella et al. (2018), Madden et al. (2020), and Vizgan et al. (2022).

Table 3: The best-fit scaling relations between the [C II] luminosity and the SFR (averaged over the last 200 Myr, SFR_{200}) and the molecular gas mass (M_{mol}) in our simulated galaxies at different redshifts.

z	No. of galaxies	$\log(L_{[\text{C II}]} / L_{\odot}) = a \log(SFR_{200} / M_{\odot} \text{ yr}^{-1}) + b$			$\log(L_{[\text{C II}]} / L_{\odot}) = a \log(M_{\text{mol}} / M_{\odot}) + b$		
		a	b	1σ	a	b	1σ
7	330	0.947 ± 0.034	6.670 ± 0.016	0.29	0.580 ± 0.034	1.893 ± 0.277	0.38
6	692	0.907 ± 0.018	6.786 ± 0.009	0.24	0.624 ± 0.018	1.690 ± 0.148	0.32
5	1210	0.852 ± 0.011	6.905 ± 0.007	0.22	0.695 ± 0.013	1.223 ± 0.108	0.30
4	2787	0.921 ± 0.006	6.985 ± 0.004	0.21	0.772 ± 0.006	0.742 ± 0.052	0.25
3	4458	0.805 ± 0.004	7.205 ± 0.003	0.18	0.733 ± 0.004	1.160 ± 0.032	0.20

The molecular gas mass, M_{mol} , is obtained by scaling up the H_2 mass directly obtained from the simulations by 1.36 to account for the contribution of helium and heavier elements confined with H_2 . At each redshift, we perform an ordinary least squares regression to fit a linear relation of the form: $\log(L_{[\text{C II}]} / L_{\odot}) = a \log(M_{\text{mol}} / M_{\odot}) + b$ to our galaxies. The corresponding best-fit parameters and the 1σ dispersion around the best fit are listed in Table 3. We observe that the slope increases with time from $z = 7$ to $z = 4$ and thereafter decreases slightly (by ≈ 0.04 dex). The overall change of ≈ 0.2 dex in the slope between $z = 7$ and $z = 3$ is similar to the change of ≈ 0.15 dex in the slope of the [C II] – SFR relation. At all redshifts, our best-fit slope is shallower than that of the Zanella et al. (2018) relation. As a result only our high-mass ($M_{\text{mol}} \gtrsim 10^9 M_{\odot}$) galaxies follow their relation, while our low-mass galaxies exhibit higher $L_{[\text{C II}]}$ than expected from extrapolation of their relation.

We also report in In Fig. 7, the Spearman’s rank correlation coefficient (ρ) between $L_{[\text{C II}]}$ and M_{mol} at each redshift. From the monotonically increasing values of ρ across redshift, we see that the [C II]- M_{mol} correlation is relatively weak at $z \gtrsim 5$ and becomes progressively stronger over time. This is in contrast with the [C II]-SFR correlation that exhibits a high value ($\rho \gtrsim 0.86$) out to $z = 7$. This trend is also evident from the decreasing values of the scatter (σ) around the best-fit linear relation between $L_{[\text{C II}]}$ and M_{mol} with decreasing redshift.

6.1. The conversion factor $\alpha_{[\text{C II}]}$

Now we compute the conversion factor between the [C II] luminosity and the molecular gas mass: $\alpha_{[\text{C II}]} \equiv M_{\text{mol}} / L_{[\text{C II}]}$ ⁴. Fig. 8 shows the correlation between $\alpha_{[\text{C II}]}$ and various galaxy properties for our simulated galaxies, namely the gas-phase metallicity, $12 + \log(\text{O}/\text{H})$, the SFR averaged over the last 5 Myr (SFR_5) and the ratio of the SFRs averaged over the last 5 and 200 Myr (hereafter R_{5-200}). The use of the latter is motivated by Lomaeva et al. (2022), who proposed an SFR change diagnostic derived from the ratio of the SFRs averaged over the past 5 and 200 Myr to quantify the current rate of change of the SFR. As different SFR indicators are sensitive to the SF happening on different timescales, their ratio can be used to quantify the SFR change over time. Lomaeva et al. (2022) proposes the ratio of $\text{H}\alpha$ to FUV emission as a proxy for SFR_5/SFR_{200} . This quantity has also been used recently to quantify the bursty SF in galaxies observed with the James Webb Space Telescope (see e.g., Atek et al. 2024; Clarke et al. 2024).

⁴ Note that the symbol α is used in Sect. 4 to denote the faint-end slope of the [C II] LF. However, throughout the text, the two are never discussed in the same context.

Table 4: Results of PCA at $z = 4$. The PCA is performed in the 5D parameter space of scaled variables as expressed in Eq. (5), where Z stands for $12 + \log(\text{O}/\text{H})$.

	M_{mol}	$L_{[\text{C II}]}$	SFR_5	SFR_{200}	Z	% of variance
PC1	0.46	0.46	0.43	0.46	0.42	88.10
PC2	-0.30	0.12	-0.60	0.10	0.72	7.33
PC3	0.05	-0.60	0.45	-0.38	0.55	3.15
PC4	-0.20	-0.57	0.03	0.80	-0.07	1.06
PC5	-0.81	0.32	0.49	0.01	0.03	0.35

In each panel of Fig. 8, we show the median $\alpha_{[\text{C II}]}$ in different bins of the quantity on the x -axis along with the 16-84 percentile range (denoted by error bars). Firstly, we observe that the $\alpha_{[\text{C II}]}$ values span about two orders of magnitude at all redshifts, particularly at $z \gtrsim 6$. The Spearman’s rank correlation coefficient (denoted by ρ) for the galaxy sample at different redshifts is reported in each panel. We find a weak correlation between $\alpha_{[\text{C II}]}$ and gas metallicity at all redshifts and observe a large scatter at all values of $12 + \log(\text{O}/\text{H})$, in agreement with Zanella et al. (2018) who found little systematic variation of $\alpha_{[\text{C II}]}$ with metallicity.

In the middle panel of Fig. 8, we observe that $\alpha_{[\text{C II}]}$ increases with SFR_5 at all redshifts, with the highest variation occurring at $z = 7$. At $SFR \gtrsim 10 M_{\odot} \text{ yr}^{-1}$, our $\alpha_{[\text{C II}]}$ values at all redshifts are in good agreement with the range from Zanella et al. (2018), but deviate towards lower values at lower SFRs. Therefore, using a constant $\alpha_{[\text{C II}]}$ (calibrated on the high-SFR galaxies alone) would lead to an overestimate of the molecular gas mass in low-SFR galaxies. A similar trend is observed in the $\alpha_{[\text{C II}]}-R_{5-200}$ plane, with $\rho \in [0.68, 0.83]$. Interestingly, in this case the correlation is the strongest at high redshifts and slowly decays at lower redshifts, highlighting the increased sensitivity of $\alpha_{[\text{C II}]}$ on the star-formation history of galaxies at $z \gtrsim 6$, as quantified by SFR change parameter R_{5-200} .

6.2. Secondary dependence of the [C II]- M_{mol} relation

After examining how $\alpha_{[\text{C II}]}$ varies with other galaxy properties, we now develop a prescription for inferring the molecular gas mass of a galaxy from its [C II] emission, taking into account these secondary dependences. For this, we perform a principal component analysis (PCA) in the 5D space of parameters – M_{mol} , $L_{[\text{C II}]}$, SFR_5 , SFR_{200} and $12 + \log(\text{O}/\text{H})$. PCA identifies dominant patterns and correlations between the parameters, reducing the dimensionality while approximately preserving variance. This technique has been previously used to identify secondary

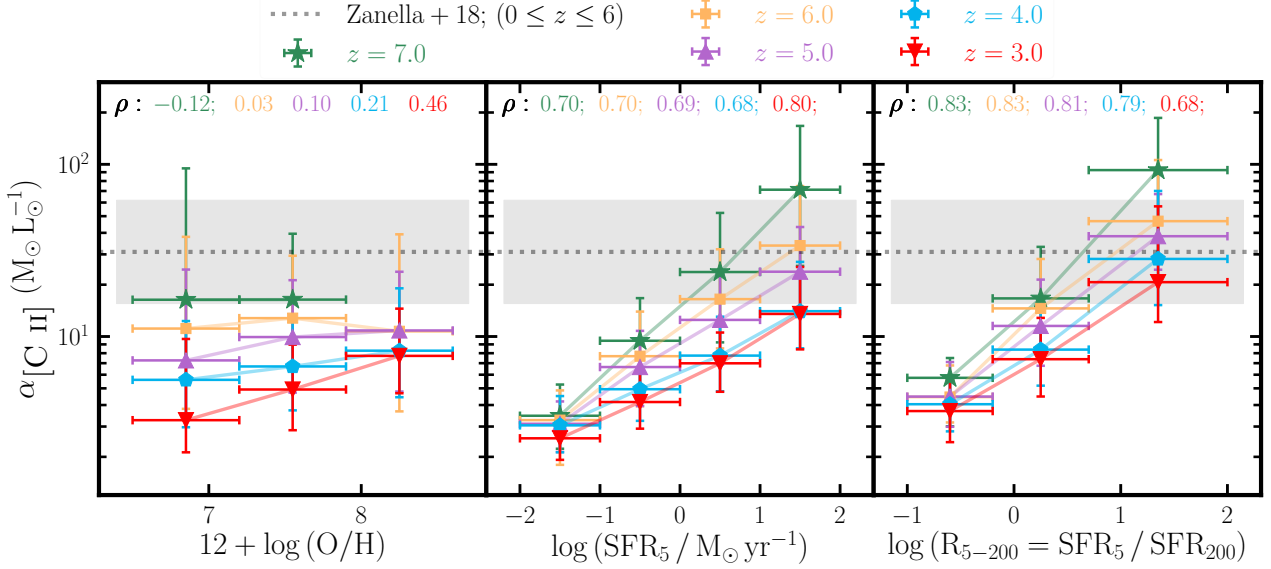


Fig. 8: The conversion factor $\alpha_{[\text{C II}]}$ in our simulated galaxies as a function of gas metallicity (left), the SFR averaged over the last 5 Myr (middle) and the SFR change diagnostic R_{5-200} (right, see text) at different redshifts. The coloured symbols represent the median $\alpha_{[\text{C II}]}$ in each bin, while the error bars represent the 16-84 percentiles. The Spearman's rank correlation coefficient between the variables on the y and x axes are shown in each panel as well. The grey dotted line denotes the mean $\alpha_{[\text{C II}]}$ from Zanella et al. (2018) and the shaded band represents the corresponding scatter.

Table 5: Coefficients for the PCA-based prescriptions for estimating the molecular gas mass at different redshifts using the equation: $\log(M_{\text{mol}}/M_{\odot}) = a \log(L_{[\text{C II}]} / L_{\odot}) + b \log(\text{SFR}_5 / M_{\odot} \text{ yr}^{-1}) + c \log(\text{SFR}_{200} / M_{\odot} \text{ yr}^{-1}) + d [12 + \log(\text{O}/\text{H})] + e$. Errors on the coefficients are obtained from bootstrapping with replacement with a 1000 iterations. The seventh and eighth columns enlist the standard deviation of the offset between the true and predicted M_{mol} when using the PCA-based and the best fit $M_{\text{mol}}-L_{[\text{C II}]}$ relations, respectively (see Fig. 9), while the last two (denoted by a *) enlist the same when accounting for typical observational uncertainties (see text).

z	a	b	c	d	e	1 σ dispersion (dex)			
						PCA	$M_{\text{mol}}-L_{[\text{C II}]}$	PCA*	$M_{\text{mol}}-L_{[\text{C II}]}$ *
7	0.50 ± 0.15	0.79 ± 0.08	-0.16 ± 0.31	$+0.04 \pm 0.26$	4.39 ± 2.80	0.20	0.45	0.28	0.47
6	0.42 ± 0.08	0.73 ± 0.02	-0.02 ± 0.10	-0.03 ± 0.07	5.46 ± 0.87	0.17	0.41	0.24	0.42
5	0.45 ± 0.04	0.65 ± 0.01	-0.00 ± 0.04	-0.03 ± 0.03	5.27 ± 0.35	0.13	0.36	0.2	0.37
4	0.47 ± 0.03	0.59 ± 0.01	$+0.01 \pm 0.03$	$+0.09 \pm 0.02$	4.11 ± 0.26	0.13	0.30	0.2	0.32
3	0.57 ± 0.02	0.59 ± 0.01	-0.06 ± 0.02	$+0.13 \pm 0.02$	3.12 ± 0.17	0.11	0.25	0.19	0.28

dependencies in the stellar-mass-metallicity relation on SFR and other parameters (Mannucci et al. 2010; Lara-López et al. 2010; Hunt et al. 2012; Bothwell et al. 2016).

Since PCA is highly sensitive to extremes in the data, we first scale all parameters by their respective mean and standard deviation before performing the analysis such that for a parameter X ,

$$X^{\text{scaled}} = \frac{\log X - \langle \log X \rangle}{\sqrt{\text{variance}(\log X)}}. \quad (5)$$

The results of this analysis are shown in Table 4. About 88% of the variance is explained by the first principal component and $\sim 95\%$ is explained by the first two principal components. The first component contains nearly equal contributions from all variables, while PC2 is dominated by metallicity. The last principal component, PC5 is dominated by M_{mol} while containing only 0.35% of the sample variance. Therefore, we set PC5 to zero to obtain an expression for M_{mol} in terms of the other quantities:

$$\begin{aligned} \log(M_{\text{mol}}/M_{\odot}) = & 4.11 + 0.47 \log(L_{[\text{C II}]} / L_{\odot}) \\ & + 0.59 \log(\text{SFR}_5 / M_{\odot} \text{ yr}^{-1}) + 0.01 \log(\text{SFR}_{200} / M_{\odot} \text{ yr}^{-1}) \\ & + 0.09 [12 + \log(\text{O}/\text{H})]. \quad (6) \end{aligned}$$

The M_{mol} obtained from Eq. (6) versus the true M_{mol} is shown in Fig. 9. We also contrast this with the M_{mol} obtained from the best-fit relation between M_{mol} and $L_{[\text{C II}]}$ ⁵. The latter shows ≈ 2.3 times higher scatter. The 1σ standard deviation between the true M_{mol} and the predicted M_{mol} using the PCA-based relation is 0.13 implying that for most (95%) of the galaxies, the PCA relation predicts the true molecular gas within a factor of ~ 1.8 while using the two variable linear best-fit, the molecular gas mass is predicted within a factor of 4. It is worth noting that

⁵ Note that this best fit is different from the one listed in Table 3 as the dependent and independent variables are reversed.

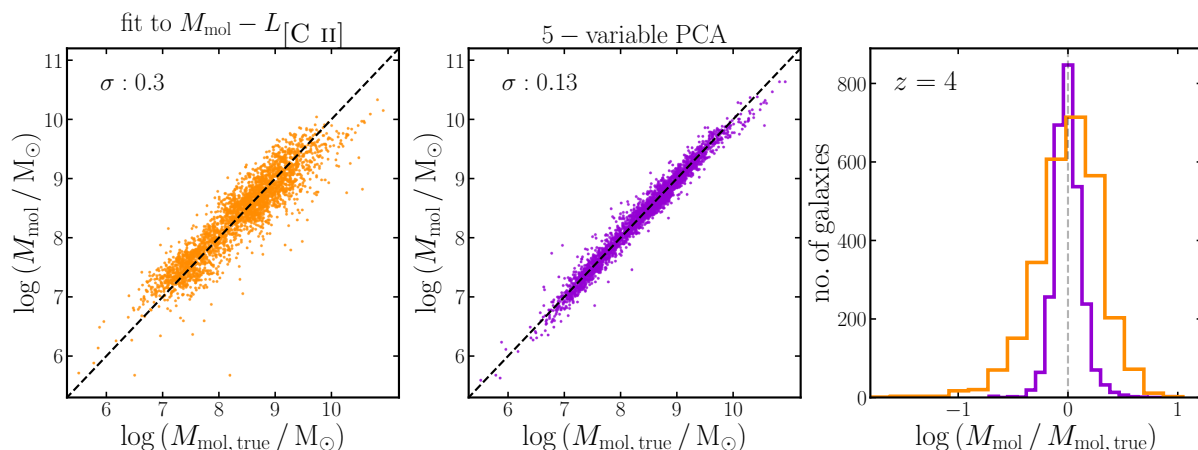


Fig. 9: Comparison of the predicted molecular gas mass estimates with the true molecular gas mass using two different approaches for simulated galaxies at $z = 4$. The left panel shows the performance of the best-fit relation between M_{mol} and $L_{[\text{C II}]}$, while the middle panel shows the same using the PCA-based relation (Table 5). In the top left corner, σ denotes the standard deviation of the offset between the true and predicted M_{mol} (both in log scale). The right panel compares the distribution of the offsets from the two approaches.

while the linear relation systematically underpredicts M_{mol} for $M_{\text{mol}} \gtrsim 10^{10} M_{\odot}$ (as the linear fit is heavily influenced by the more numerous low-mass galaxies), the PCA-based prediction does not suffer from this discrepancy.

We obtain similar results at other redshifts; these are listed in Table 5. To estimate the uncertainties in the coefficients of the PCA-based relation, we perform a bootstrapping analysis with replacement, using 1000 iterations at each redshift. We find that the coefficient a , that quantifies the dependency of M_{mol} on $L_{[\text{C II}]}$, increases from $z = 6$ to $z = 3$, while the coefficient b , that represents the dependency of M_{mol} on SFR_5 decreases such that at $z = 3$, $a \approx b$. Interestingly, the dependence of M_{mol} on SFR_{200} and metallicity is relatively low at all times and does not evolve significantly with redshift.

6.2.1. Accounting for observational uncertainties

To estimate the impact of observational uncertainties in measurements of $L_{[\text{C II}]}$, SFR_5 , SFR_{200} , and $12 + \log(\text{O}/\text{H})$ in estimating M_{mol} , we add a random perturbation, δ , to each of the four quantities, where δ is drawn from a normal distribution with a mean of zero and a standard deviation corresponding to the typical errors reported in observations of high- z galaxies. For instance we adopt an error of 0.1 dex for $L_{[\text{C II}]}$ and 0.24 dex for SFR_5 and SFR_{200} , both based on ALPINE galaxies (B  thermin et al. 2020). For $12 + \log(\text{O}/\text{H})$, we adopt an error of 0.05 dex (Sanders et al. 2015). Then we employ the PCA-based relations shown in Table 5 to obtain a prediction for M_{mol} and compute the offset from between our prediction and the true M_{mol} . We then compute the standard deviation of this offset (as before, the offset is computed from the log of the quantities). We repeat the procedure for the best-fit $M_{\text{mol}} - L_{[\text{C II}]}$ relation. The resulting σ values are reported in the last two columns of Table 5. Overall, even accounting for observational uncertainties, the PCA-based relation provides a significant gain in the precision/accuracy of molecular gas mass estimates and is capable of predicting the true molecular gas mass within a factor of 2 at $3 \leq z \leq 6$.

6.3. Correlation with other quantities

In addition to the SFR and the molecular gas mass, the [C II] emission at high redshifts has been shown to correlate with the metal mass in the gas-phase of high- z galaxies (Heintz et al. 2023). In Khatri et al. (2024), we found that the C^+ distribution in our post-processed galaxy shows a greater similarity with the total gas distribution while CO and atomic carbon correlate better with the molecular gas. Inspired by these findings, we further investigate the correlation between $L_{[\text{C II}]}$ and the total gas mass (M_{gas}) and the mass in metals (M_{metal}). At each redshift, we perform an ordinary least squares regression and the resulting parameters and the 1σ scatter around the best fit are listed in Table 6.

We find that among the galaxy properties explored so far, namely the SFR, the molecular gas mass, the total gas mass, and the metal mass, the [C II] emission in our simulated galaxies shows the strongest/tightest correlation with M_{metal} across redshifts. This is evident from the lowest scatter in this relation. In other words, we can say that the gas-phase metal mass is the most robust predictor of the [C II] emission in any given galaxy. Interestingly, the scatter in the $L_{[\text{C II}]} - M_{\text{metal}}$ relation is lower than the scatter in the $L_{[\text{C II}]} - M_{\text{gas}}$ relation at all times. A stronger correlation between [C II] emission and total gas mass simply highlights the multi-phase origin of the emission.

After exploring the correlation between $L_{[\text{C II}]}$ and other galaxy properties in our simulations, we now turn our attention to examining the spatial extent of the [C II] emission in these galaxies and how it varies across the galaxy population.

7. Extended [C II] emission

In recent years, several observations of high- z ($z \gtrsim 4$) galaxies have revealed that the [C II] emission extends 2 – 3 times farther than the UV continuum emission. These findings come from both stacked galaxy samples (e.g., Fujimoto et al. 2019; Ginolfi et al. 2020; Fudamoto et al. 2022) and individual galaxies (e.g., Fujimoto et al. 2020; Lambert et al. 2023; Posses et al. 2024), with some studies, like Posses et al. (2024), resolving emission on ~ 1 kpc scales within galaxies. Potential sources of this extended emission include unresolved satellites, outflows, and extended

Table 6: The best-fit scaling relations between the [C II] luminosity and the total gas mass (M_{gas}) and the metal mass in the gas phase (M_{metal}) in our simulated galaxies at different redshifts.

z	$\log(L_{[\text{C II}]} / L_{\odot}) = a \log(M_{\text{gas}} / M_{\odot}) + b$			$\log(L_{[\text{C II}]} / L_{\odot}) = a \log(M_{\text{metal}} / M_{\odot}) + b$		
	a	b	1σ	a	b	1σ
7	1.080 ± 0.032	-3.437 ± 0.298	0.25	0.888 ± 0.016	-0.379 ± 0.128	0.17
6	1.064 ± 0.019	-3.209 ± 0.179	0.22	0.851 ± 0.009	-0.044 ± 0.072	0.14
5	1.116 ± 0.014	-3.641 ± 0.132	0.22	0.843 ± 0.005	$+0.048 \pm 0.045$	0.12
4	1.193 ± 0.006	-4.169 ± 0.057	0.16	0.851 ± 0.003	$+0.059 \pm 0.024$	0.11
3	1.158 ± 0.004	-3.753 ± 0.040	0.14	0.798 ± 0.002	$+0.481 \pm 0.018$	0.10

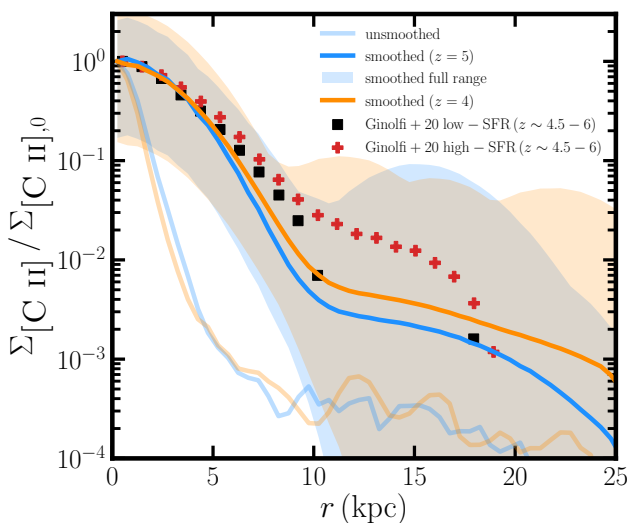


Fig. 10: Comparison of the simulated and observed stacked (radial) surface brightness profiles of the [C II] emission. The observed profiles are from [Ginolfi et al. \(2020\)](#) for two samples of 25 galaxies each from the ALPINE survey at $z = 4.5 - 5.9$ – a low-SFR ($\text{SFR} < 25 M_{\odot} \text{yr}^{-1}$, black squares) sample and high-SFR ($\text{SFR} \geq 25 M_{\odot} \text{yr}^{-1}$, red pluses) sample. The solid lines represent the stacked profiles of the 50 highest star-forming (central) galaxies from the simulation at $z = 5$ (in blue) and $z = 4$ (in orange). The shaded areas represent the full range spanned by the individual profiles, which are constructed from the 2D projection of a 50 kpc cube centred on the galaxy along three orthogonal lines of sight. All profiles are smoothed with a 2D Gaussian beam of FWHM $0.9''$ (as in [Ginolfi et al. \(2020\)](#)) and normalized by the peak value of the stack. For reference, the unsmoothed stacked profiles are shown in lighter shades.

PDRs (see, e.g., Figure 12 in [Fujimoto et al. 2019](#)). In [Khatri et al. \(2024\)](#), we examined the extent of C^+ in a simulated galaxy by calculating the H_2 , CO, C, and C^+ abundances in post-processing using the sub-grid model HYACINTH, and found that the C^+ surface density profile is more extended than other components such as H_2 and CO, and closely resembles the total gas distribution and that of young stars (with ages ≤ 20 Myr). Here we extend our analysis to a statistical sample of galaxies from the MARIGOLD suite and examine the extent of their [C II] emission. For this, we first look at the stacked emission from a sample of galaxies at two different redshifts (Sect. 7.1). Then we inspect the relative extent of the [C II] emission with respect to SF in in-

dividual galaxies and investigate possible causes of an extended [C II] emission (Sect. 7.2).

7.1. Stacked [C II] emission

In this section, we compare the stacked [C II] emission from our simulated galaxies with that from [Ginolfi et al. \(2020\)](#) based on 50 [C II]-detected galaxies from ALPINE at $z = 4.5 - 5.9$. The stacked [C II] emission from these galaxies extends out to ~ 15 kpc. The authors further split their sample into low star-forming ($\text{SFR} < 25 M_{\odot} \text{yr}^{-1}$) and high star-forming ($\text{SFR} \geq 25 M_{\odot} \text{yr}^{-1}$ galaxies) and reported that the extended [C II] emission is more prominent in the latter.

To compare with these observations, we selected the top 50 highest star-forming (central) galaxies each at redshifts $z = 4$ and $z = 5$. For each galaxy, we obtained the [C II] surface brightness map from the 2D projection of a cylinder centred on the galaxy with a line-of-sight velocity cut of $v_{\text{los}} \in [-200, 200] \text{ km s}^{-1}$ (same as in [Ginolfi et al. 2020](#)) along three orthogonal lines of sights (these are taken to be the coordinate axes of the simulation box). Note that in this analysis, we adopted the stellar centre of the galaxy to be the spatial centre of the [C II] emission⁶. We smoothed the resulting surface brightness maps with a 2D Gaussian beam of FWHM $0.9''$ to mimic the synthesized ALMA beam in [Ginolfi et al. \(2020\)](#). We then stack the individual smoothed surface brightness maps. Note that, since we do not add noise to the galaxy images, our stacking procedure is unweighted by construction and is different from the variance-weighted stacking employed in observations.

From the stacked surface brightness map at each redshift, we extract radial profiles in bins of size 0.5 kpc. The resulting profiles are shown as solid lines in Fig. 10. The shaded areas represent the full range covered by the individual profiles. We also include for reference, the profiles obtained without smoothing using a faint line of the same colour. We see that while the true [C II] distribution in the simulated galaxies is rather compact, smoothing extends the profiles out to larger radii. We observe that our stacked profiles show a remarkable agreement with the [Ginolfi et al. \(2020\)](#) profile for their low-SFR sample. However our stacked profile is not as extended as their high-SFR sample. Nevertheless, some individual galaxies exhibit a similar extent as the high-SFR [Ginolfi et al. \(2020\)](#) profile (as indicated by the spread of our stacked profiles).

⁶ Note that the centres of the different baryonic components do not necessarily overlap. However, since we apply Gaussian smoothing to the surface brightness maps with a $0.9''$ beam, which is equivalent to 6.4 kpc (5.5 kpc) at $z = 5$ ($z = 4$), we do not expect this offset to significantly impact our results.

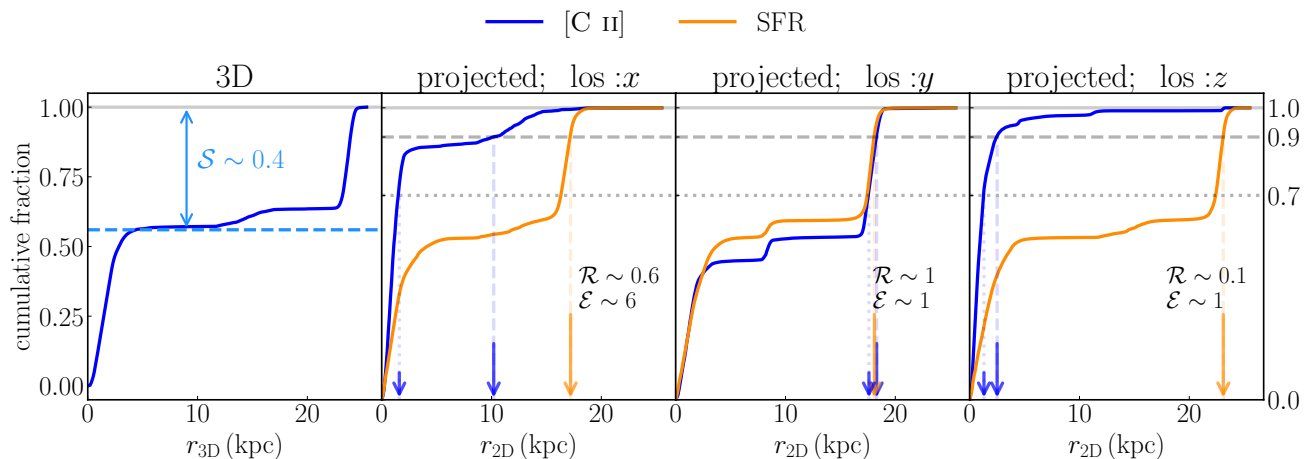


Fig. 11: An example illustrating the calculation of the \mathcal{S} , \mathcal{R} , and \mathcal{E} parameters in a simulated galaxy. The left panel shows the cumulative profile for the 3D distribution of [C II], with the dashed line marks the contribution of the central galaxy to the total [C II] emission (as evident from the flattening of the cumulative profile). The remaining fraction (denoted by \mathcal{S}) represents the contribution of satellites. The other panels show cumulative profile constructed from the [C II] surface brightness (blue) and SFR surface density (orange). For the profiles obtained from projections, the value of the \mathcal{R} and \mathcal{E} parameters are indicated in each panel. In all but the leftmost panel, the dotted, dashed and solid horizontal lines denote cumulative fractions of 70%, 90%, and 100%, respectively. The small and large blue arrows mark $r_{70, [\text{C II}]}$ and $r_{90, [\text{C II}]}$, respectively and the orange arrow denotes $r_{90, \text{SFR}}$. The parameters $\mathcal{R} \equiv r_{90, [\text{C II}]} / r_{90, \text{SFR}}$ is calculated from the ratio of the r values denoted by the large blue and orange arrows, while the parameter $\mathcal{E} \equiv r_{90, [\text{C II}]} / r_{70, [\text{C II}]}$ from the ratio of the large and small blue arrows.

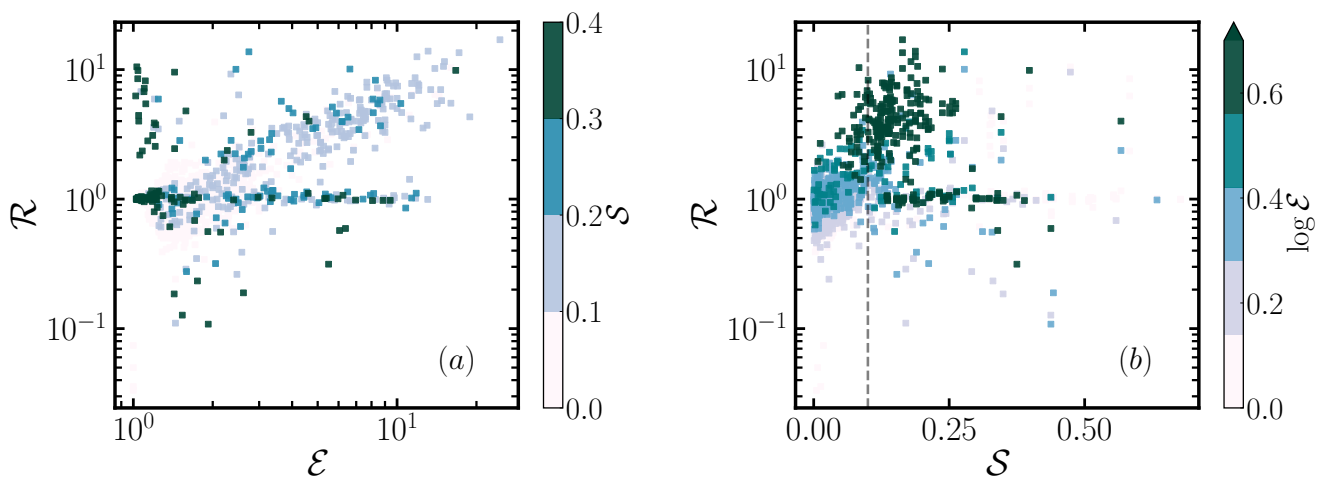


Fig. 12: The distribution of our galaxies at redshift $z = 4$ in the \mathcal{R} - \mathcal{E} (left), \mathcal{R} - \mathcal{S} (right) planes. The scatter points are colour-coded by the parameter \mathcal{S} in the left panel and by the log of parameter \mathcal{E} in the right panel. The dashed grey lines in the right panel indicates the threshold value of \mathcal{S} used to separate galaxies into low and high \mathcal{S} .

7.2. Extent of [C II] emission in individual objects

Now we aim to quantify the extent of the [C II] emission relative to the SF activity in our simulated galaxies. For this analysis, we include all galaxies that meet the following criteria: (i) $M_* \geq 10^{8.5} M_\odot$ and (ii) $\text{SFR} \geq 3 M_\odot \text{ yr}^{-1}$. These are chosen to match the range of M_* and SFR values in ALPINE galaxies (Le Fèvre et al. 2020). For each galaxy in our sample, we take a sphere of radius 25 kpc centred on the galaxy and obtain projections of the same along three orthogonal lines of sights (we take these to be the coordinate axes of the simulation box) to obtain the [C II] surface brightness and SFR surface density maps. Then we compute the (cumulative) radial surface brightness profiles for each projection, from which we derive the radius enclosing 70%

and 90% of the total [C II] emission – these are denoted as $r_{70, [\text{C II}]}$ and $r_{90, [\text{C II}]}$, respectively. Similarly, from the (cumulative) SFR surface density profile, we derive $r_{90, \text{SFR}}$ (as in Sect. 5, we use the SFR averaged over the last 200 Myr). For each galaxy, we also compute the cumulative [C II] luminosity profile from the full 3D distribution of [C II] within the region.

Based on these, we calculate the following parameters for each galaxy for the three orthogonal projections. As an example, we show in Fig. 11, cumulative profiles for a simulated galaxy and how these are used for calculating the three parameters and to ease their interpretation.

1. The multicomponent extent parameter $\mathcal{E} \equiv r_{90, [\text{C II}]} / r_{70, [\text{C II}]}$ that measures the spread in the [C II] emission. A higher \mathcal{E} indicates a relatively larger extent of

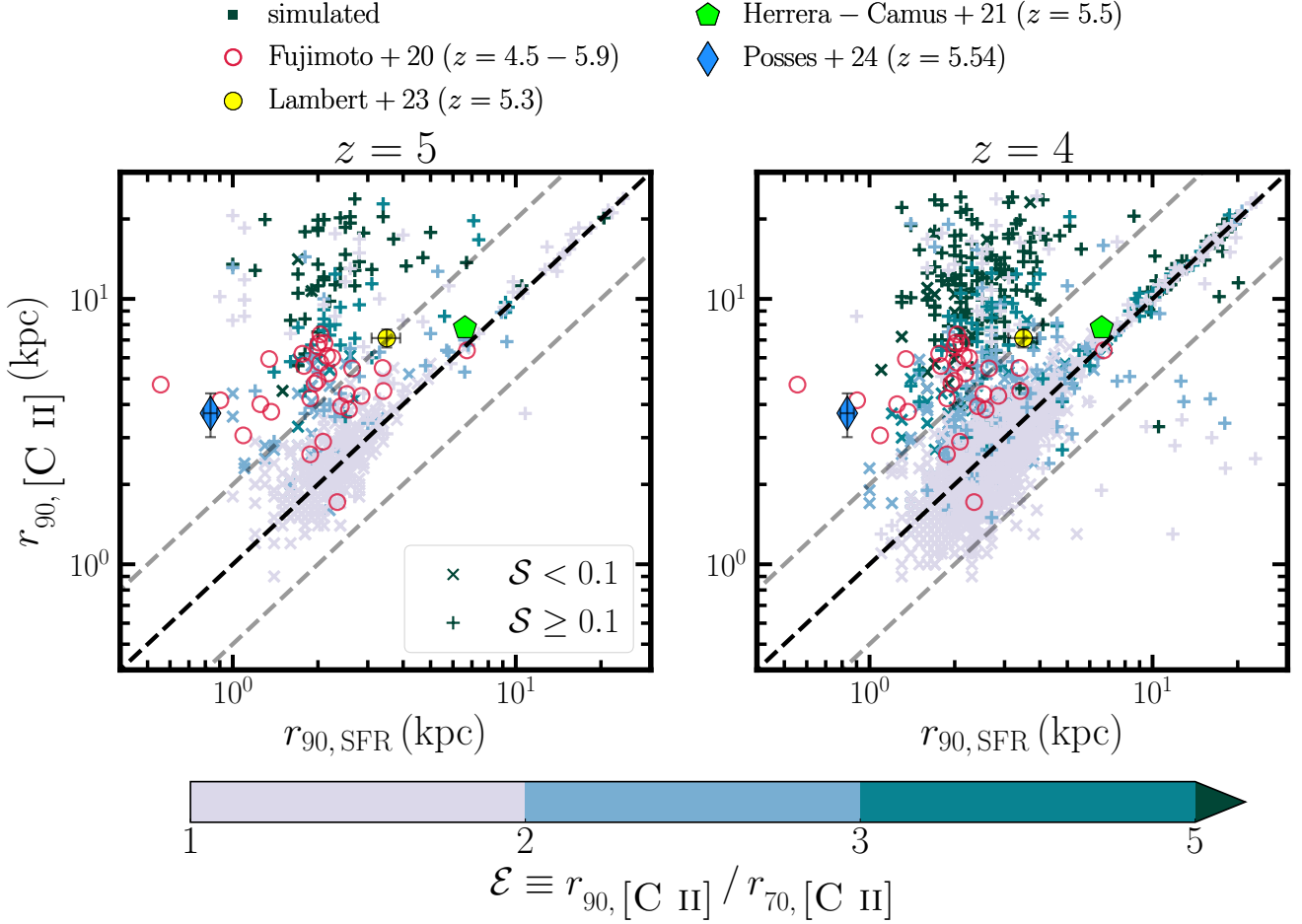


Fig. 13: Comparison of $r_{90, [\text{C II}]}$ and $r_{90, \text{SFR}}$ for simulated galaxies at redshifts $z = 5$ (left) and $z = 4$ (right). The galaxies are colour-coded by their multicomponent extent parameter \mathcal{E} defined as the ratio of the r_{90} and r_{70} values of the $[\text{C II}]$ surface brightness profile. The shape of the symbol reflects the \mathcal{S} parameter that quantifies the satellite contribution to the total $[\text{C II}]$ emission (see text for details). We use ‘low \mathcal{S} ’ and ‘high \mathcal{S} ’, respectively to denote galaxies with $< 10\%$ and $\geq 10\%$ satellite contribution. These $r_{90, [\text{C II}]}$ versus $r_{90, \text{SFR}}$ values of observed galaxies are shown as red open circles (Fujimoto et al. 2020), a yellow plus (Lambert et al. 2023), a green pentagon (Herrera-Camus et al. 2021), and a blue diamond (Posses et al. 2024). The black dashed line indicates a 1:1 relation, while the top and bottom grey dashed lines indicate 2:1 and 1:2 relations, respectively. Note that the error bars are not shown for Fujimoto et al. (2020) galaxies for the sake of clarity.

the diffuse $[\text{C II}]$ component. This would occur in galaxies where 70% of the emission is relatively confined, while the remaining 10 – 30% is more spread out, likely due to the presence of satellite galaxies. Thus, a higher \mathcal{E} denotes more extended emission relative to the bulk of the emission.

2. The parameter $\mathcal{R} \equiv r_{90, [\text{C II}]} / r_{90, \text{SFR}}$ that quantifies the relative extent of the $[\text{C II}]$ emission compared to SF. In this analysis, we are particularly interested in galaxies where the $[\text{C II}]$ emission is at least twice as extended as the SF activity (i.e., $\mathcal{R} \geq 2$).
3. The parameter \mathcal{S} that quantifies the fraction of the total $[\text{C II}]$ emission that arises from outside the central galaxy and represents the contribution from satellites. Unlike, \mathcal{R} and \mathcal{E} , this parameter is computed from the true 3D distribution of $[\text{C II}]$ emission and is therefore agnostic to the projection axis by construction.

Note that all three parameters are agnostic to whether the $[\text{C II}]$ emission at a given location represents a C^+ ion formed in situ or transported there, e.g., via outflows/inflows.

From Fig. 11, it is evident that the parameters \mathcal{R} and \mathcal{E} are sensitive to the orientation of the galaxy. For instance, the y -

projection of the galaxy has $\mathcal{R} \sim 1$, indicating equal extent of the $[\text{C II}]$ emission and SFR. In contrast, in the x - and z - projections, the SFR profile is more extended than the $[\text{C II}]$ profile, resulting in $\mathcal{R} < 1$. Note that in this case the \mathcal{E} value is relatively high, i.e., the $r_{70, [\text{C II}]}$ and $r_{90, [\text{C II}]}$ are well separated, but owing to a more extended SFR profile, the \mathcal{R} value is low.

To better understand how the three parameters are correlated, we show in Fig. 12, how \mathcal{R} varies with \mathcal{E} and \mathcal{S} for our galaxy sample at $z = 4$. Each scatter point represents one of the orthogonal projections of a galaxy and is colour-coded by value of the third parameter. Firstly, in panel (a), we see that the parameter \mathcal{R} increases in general with \mathcal{E} . However, some galaxies⁷ with $\mathcal{R} \geq 2$ exhibit a low $\mathcal{E} (\leq 2)$. In contrast, in panel (b), we see that all galaxies with a high \mathcal{R} generally have a high \mathcal{S} as well, although the reverse is not always true – some galaxies have a high \mathcal{S} but $\mathcal{R} \sim 1$. In these galaxies, satellites contribute similarly to the $[\text{C II}]$ emission and the SF, driving the r_{90} of both quantities

⁷ Note that while \mathcal{R} and \mathcal{E} are properties of the projection of a given galaxy, for simplicity, we associate these parameters directly with the galaxy itself.

to high values, and thereby reducing the \mathcal{R} (the y -projection in Fig. 11 is an example of this).

In Fig. 13, we compare the extent of the r_{90} values of the [C II] emission and the SFR. The galaxies are colour-coded according to their \mathcal{E} parameter while the shape of the symbol represents the value of the \mathcal{S} parameter: we split the galaxies into ‘low \mathcal{S} ’ ($\mathcal{S} < 0.1$) and ‘high \mathcal{S} ’ ($\mathcal{S} \geq 0.1$) subsamples. The threshold of 0.1 or 10% is inspired by Springel et al. (2008) who found that $\approx 11\%$ of the mass fraction in virialized haloes is present in substructures. For reference, we also show the r_{90} values for [C II] and SFR from observations of individual galaxies: to obtain these, we use the half-light radii r_e for the [C II] emission and UV continuum emission, reported in the respective observations. In all observations shown in Fig. 13, $r_{e, [C II]}$ and $r_{e, UV}$ are obtained from fitting exponential disk-profiles to the [C II] emission and UV continuum emission, respectively. We scale these r_e values by 2.318 to obtain the respective r_{90} values⁸. Since the bulk of the UV emission from galaxies arises from stars younger than ≈ 100 Myr (Kennicutt & Evans 2012), we further assume that the $r_{90, SFR}$ in the observed galaxies can be approximated by the $r_{90, UV}$ values. A possible caveat is that the UV sizes might be larger than the corresponding SFR sizes (e.g., see Szomoru et al. 2013, for a comparison of the half-light and half-mass radii of $0.5 < z < 2$ galaxies.).

From Fig. 13, we see that the [C II] emission in many of our simulated galaxies have a similar extent as the observed galaxies at $4.5 \lesssim z \lesssim 5.9$ from Fujimoto et al. (2020), Herrera-Camus et al. (2021), and Lambert et al. (2023). However, our simulated galaxies occupy a larger area of the parameter space compared to observations. Our galaxies where the [C II] emission is at least twice as extended as the SF activity (i.e., above the top grey dashed line, $\mathcal{R} \geq 2$) exhibit preferentially higher \mathcal{E} values (darker colours of the symbol) and a higher contribution from satellites, compared to galaxies lying along the diagonal (i.e. $\mathcal{R} \sim 1$). This is also evident from the higher median of the \mathcal{E} and \mathcal{S} parameters for the galaxies with $\mathcal{R} \geq 2$ (see Table 7).

To summarize, we find that the inferred detection of an extended [C II] emission in a given galaxy is sensitive to the orientation of the galaxy. Nevertheless, some statistical differences emerge between galaxies with extended [C II] emission compared to their SF activity (i.e., with $\mathcal{R} \equiv r_{90, [C II]} / r_{90, SFR} \geq 2$) and those without (i.e., $\mathcal{R} < 2$). Galaxies with $\mathcal{R} \geq 2$ tend to have a higher contribution from satellites. They also exhibit higher \mathcal{E} values compared to the latter, indicating that while the bulk ($\sim 70\%$) of the [C II] emission is relatively concentrated, the remaining fraction can extend out to 4-5 times larger radii. Overall, about 10% of our simulated galaxies at $z = 4$ have $\mathcal{R} \geq 2$ i.e., their [C II] emission extends ≥ 2 times farther than the SF activity; this fraction increases to 20% at $z = 5$. This is in agreement with recent observations pointing out the increased prevalence of extended [C II] emission towards higher redshifts (Carniani et al. 2018; Fujimoto et al. 2019; Ginolfi et al. 2020; Fudamoto et al. 2022).

8. Comparison with previous work

In Fig. 14, we compare our best-fit [C II]-SFR relation (Table 3) with previous numerical work in the literature, briefly described in the following. Lagache et al. (2018) used a semi-analytical galaxy-formation model coupled to the photoionisation code

⁸ We remind the reader that for an exponential disk-profile $\Sigma = C \exp(-r/h)$, where h is the scale length of the disk, the half-light radius $r_e \approx 1.678 h$ and $r_{90} \approx 3.890 h$. Therefore $r_{90} \approx 2.318 r_e$.

Table 7: Median values of the parameters \mathcal{E} and \mathcal{S} for galaxies with and without extended [C II] emission at $z = 4$ and $z = 5$.

	$z = 4$		$z = 5$	
	median \mathcal{E}	median \mathcal{S}	median \mathcal{E}	median \mathcal{S}
$\mathcal{R} \geq 2$	5.5	0.14	3.99	0.17
$\mathcal{R} < 2$	1.5	0.02	1.5	0.03

CLOUDY (Ferland et al. 1992) to obtain the [C II] luminosity for a statistical sample of galaxies at redshifts $4 \leq z \leq 8$. From their full sample of galaxies, they obtain a [C II]-SFR relation of the form: $\log(L_{[C II]}/L_{\odot}) = (1.4 - 0.07z)\log(\text{SFR}/M_{\odot} \text{ yr}^{-1}) + 7.1 - 0.07z$, which is shown as solid lime line in the figure. In their galaxies, Vallini et al. (2015) calculated the [C II] emission from a single $z \sim 7$ galaxy from a high-resolution (≈ 60 pc) SPH simulation (Pallottini et al. 2014) assuming optically-thin emission. To do so, they adopt a log-normal sub-grid density distribution with a variable Mach number. In this regard, their approach is similar to ours except that we adopt a log-normal+power-law PDF in regions where self-gravity cannot be neglected (see Khatri et al. 2024, for details). They investigate how the total [C II] luminosity changes with metallicity, assuming a uniform metal distribution. To derive the [C II]-SFR relation, they scale the [C II] luminosity with the molecular gas mass ($L_{[C II]} \propto M_{H_2}$), which is assumed to scale with the SFR in accordance with the Kennicutt-Schmidt relation: $\Sigma_{SFR} \propto \Sigma_{H_2}^N$. In Fig. 14, we show their results for $N = 1$ (in blue) and $N = 2$ (in orange). For both cases, the dotted line is for the median gas-metallicity (Z_{gas}) of our galaxies at a given redshift, while the shaded area represents the range adopting the 16 and 84 percentiles of the metallicity distribution. Previously, Lagache et al. (2018) found that their [C II]-SFR agrees well with the one from Vallini et al. (2015) for $N = 2$. We also include the results from Leung et al. (2020) and Vizgan et al. (2022), both of which were obtained by post-processing $z \sim 6$ galaxies from the SIMBA simulations using different versions of the emission line tool SÍGAME (Olsen et al. 2015, 2017). SÍGAME includes a multi-phase ISM model and accounts for the contribution of different phases (molecular gas phase, cold neutral medium, and H II regions) to the [C II] emission of a galaxy and employs CLOUDY to obtain the chemical abundances in the different phases. For reference, we also show the [C II]-SFR relation based on observations of $0.5 \leq z \leq 6.6$ galaxies (De Looze et al. 2014) as a solid blue line with a scatter of 0.4 dex (the same is shown as a solid orange line in Fig. 5).

Overall, we see that the variation among the different models increases with redshift, and can span up to an order of magnitude at $\text{SFR} \sim 1 - 10 M_{\odot} \text{ yr}^{-1}$. This is enhanced towards lower and higher SFRs. We find that at all redshifts our [C II]-SFR relation differs significantly from Vallini et al. (2015). In this regard, while their approach for calculating the [C II] emission accounting for the sub-grid densities is similar to ours (albeit with different sub-grid density PDFs), their method to derive the [C II]-SFR relation relies on scaling relations between $L_{[C II]}$ and M_{H_2} and $\Sigma_{SFR} - \Sigma_{H_2}$, while we follow the dynamical evolution of these quantities in our simulations. Moreover, as shown by our PCA analysis (Sect. 6.2), the $L_{[C II]} - M_{\text{mol}}$ relation has secondary dependencies on the SFR, that evolve with redshift. This provides a natural explanation for the different results from the two studies. At $5 \leq z \leq 7$, our results, as well as those from Lagache et al. (2018), show slightly steeper slopes compared to those from Leung et al. (2020) and Vizgan et al. (2022). However, these differences remain within the scatter of $\sim 0.3 - 0.6$. Notably, at

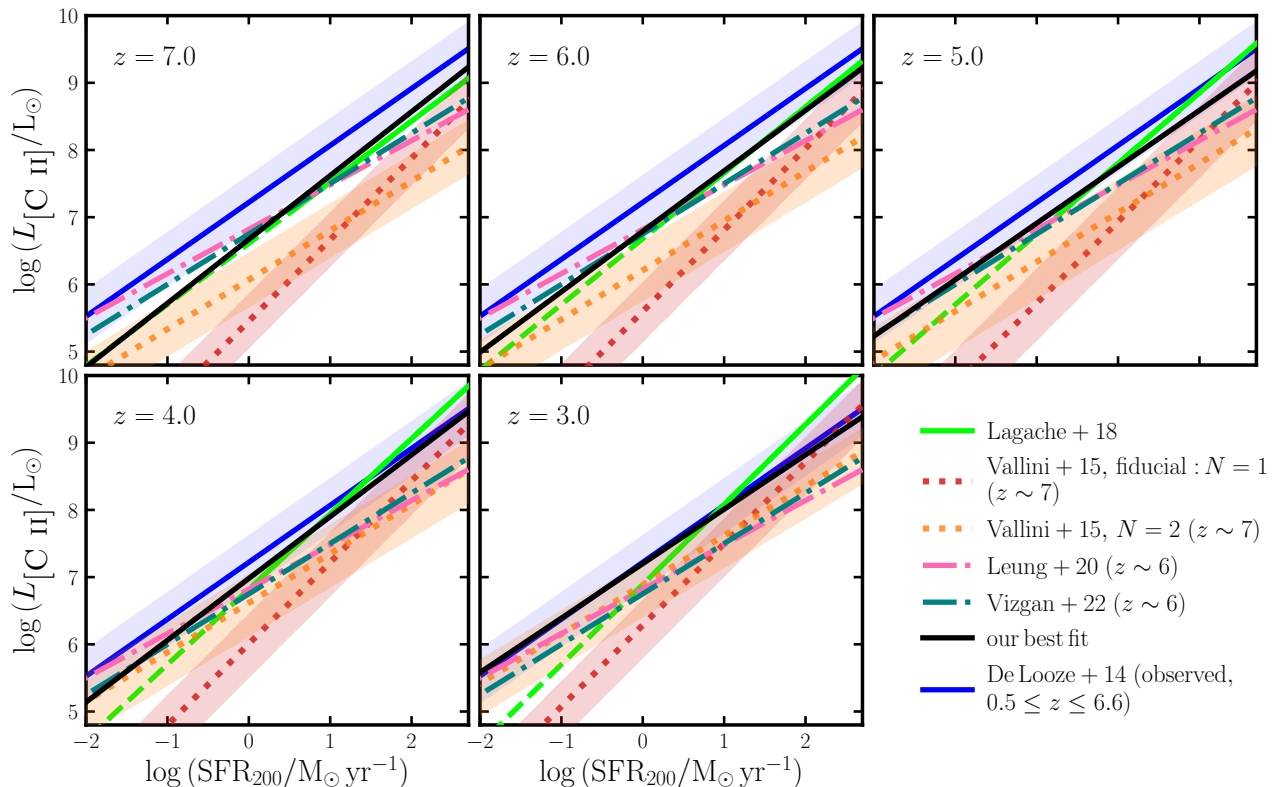


Fig. 14: Comparison of our [C II]-SFR relation (black line) at different redshifts with other relations from the literature. The relations from [Lagache et al. \(2018\)](#) are shown in lime. The red and orange dotted lines along with the scatter represent the [Vallini et al. \(2015\)](#) relations with $N = 1$ and $N = 3$, respectively for the Kennicutt-Schmidt relation. In both cases we show with the dotted line the relation assuming the median Z_{gas} of our simulated galaxies at a given redshift, while the shaded area encloses the relations with 16-84 percentile of our Z_{gas} values. The dash-dotted lines in pink and teal represent the relations from [Leung et al. \(2020\)](#) and [Vizgan et al. \(2022\)](#), respectively, both obtained by post-processing the $z \sim 6$ snapshot of the SIMBA simulations ([Davé et al. 2020](#)) with different versions of SÍGAME ([Olsen et al. 2015, 2017](#)). For reference, we include the [De Looze et al. \(2014\)](#) relation based on observations of $0.5 \leq z \leq 6.6$ galaxies as a blue line with a scatter of 0.4 dex shown by the shaded region.

these redshifts, the numerical predictions fall slightly below the empirical [De Looze et al. \(2014\)](#) relation. At $z = 3$, our best-fit shows an excellent agreement with [De Looze et al. \(2014\)](#) and exhibits a slightly higher offset compared to others except [Lagache et al. \(2018\)](#).

In Fig. 15, we compare our [C II] LF against the results from [Popping et al. \(2016\)](#) and [Lagache et al. \(2018\)](#), both based a semi-analytical galactic formation models. [Popping et al. \(2016\)](#) fit a Schechter functions to their predicted LFs at different redshifts. At $z = 6$, our predicted LF is very similar to [Popping et al. \(2016\)](#), despite the differences in our methods. However, deviations start to appear at late times. For instance, despite similar faint-end slopes at redshifts $z = 4$, our simulations predict a high number density of emitters at the all luminosities. Moreover, our LFs extend out to higher luminosities, similar to [Lagache et al. \(2018\)](#), who fit their LFs with a single power law with a slope of -1.0 at all redshifts. In this regard, the underabundance of bright galaxies in semi-analytical models (SAMs) that track the H_2 abundance is a well-known problem and is related to the underabundance of cold gas in the galaxies simulated with SAMs ([Popping et al. 2015](#)). At all redshifts, we find a steeper bright-end slope in comparison to [Lagache et al. \(2018\)](#). We further compare with the LF from [Garcia et al. \(2024\)](#) obtained by post-processing the SIMBA simulations at $z = 5$ and 6. We find that although consistent

within 1σ uncertainty, their predictions are consistently below ours and can be up to an order of magnitude lower at the bright end.

Discrepancies in the predicted LFs from different studies can have important consequences for predicting the power spectrum of the line intensity mapping (LIM) signal. LIM is an emerging technique that measures the integrated line emission from galaxies and the intergalactic medium without resolving individual sources (see [Bernal & Kovetz 2022](#), for a recent review). The first moment of the LF governs the overall amplitude of the LIM power spectrum, while the second moment influences the shot noise component. As bright emitters are expected to have a dominant contribution to the [C II] LIM power spectrum at $z \gtrsim 4$ (e.g. [Marcuzzo et al. 2025](#)), current and upcoming LIM surveys can prove extremely useful in constraining the different numerical models.

9. Summary

Based on a sample of simulated galaxies with molecular cloud chemistry evolved on the fly and [C II] $158 \mu\text{m}$ line emission calculated in post-processing, we have investigated the reliability of this line as a tracer of the SF activity and molecular gas content

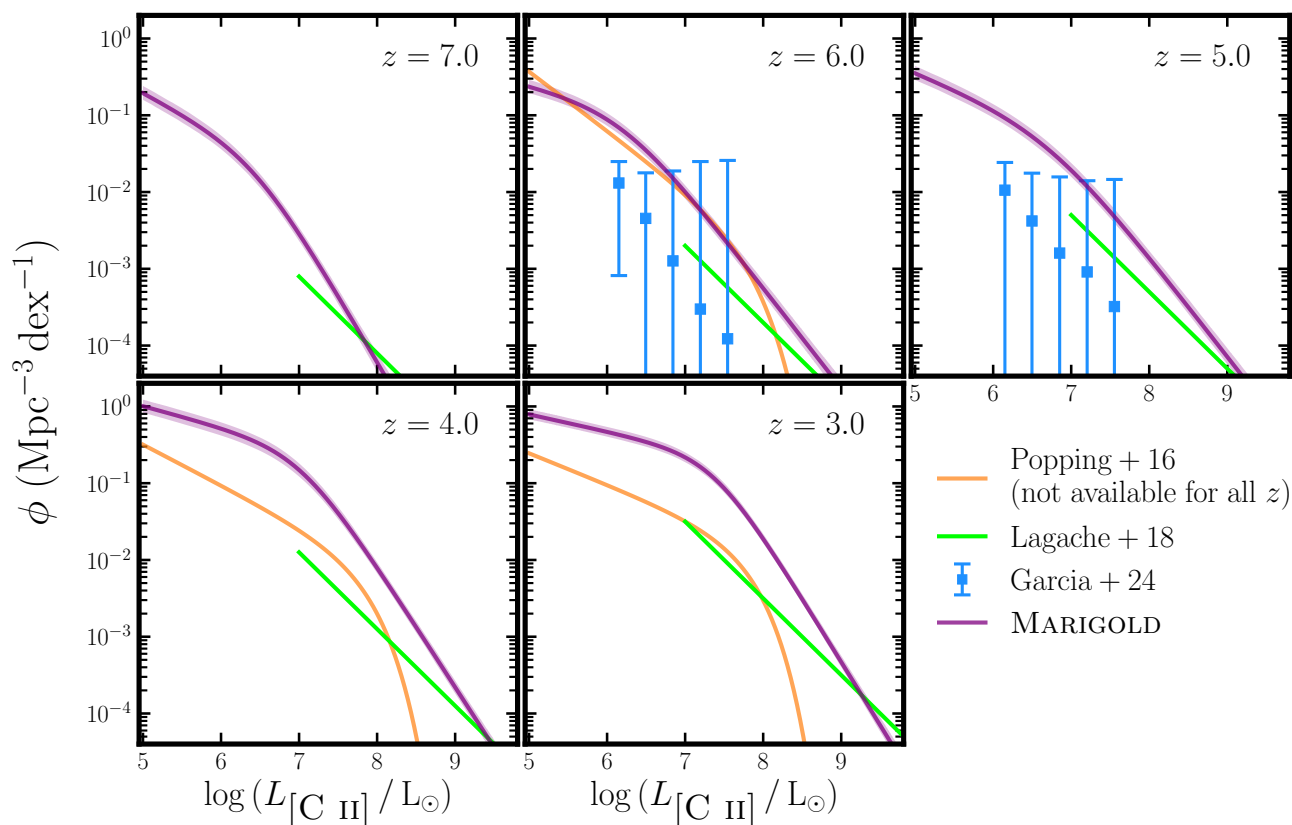


Fig. 15: Comparison of the [C II] LF from the MARIGOLD simulations at different redshifts with those from Popping et al. (2016) and Lagache et al. (2018) both based on a semi-analytical galaxy formation model, and from Garcia et al. (2024) obtained by post-processing the SIMBA simulations at $z = 6$ and 5 .

in galaxies at redshifts $3 \leq z \leq 7$. Here we briefly summarize our findings:

- Redshift evolution of the [C II] luminosity function:** Our simulations predict a strong time evolution in the number density of [C II] emitters, especially at the bright end. The number density of $L_{[\text{C II}]} \sim 10^9 L_{\odot}$ galaxies increases by 600 times in the above redshift range. At all redshifts, a double power-law provides a better fit to our simulated LFs (Table 2).
- Redshift evolution of the [C II]-SFR relation:** The slope $L_{[\text{C II}]} - \text{SFR}$ relation shows little evolution in the redshift range $3 \leq z \leq 7$ while the intercept increases by ≈ 0.5 dex in this interval, indicating that the [C II] luminosity at given SFR increase roughly by a factor of three from $z = 7$ to $z = 3$. Notably, the scatter in the relation increases towards higher redshifts (Table 3).
- The conversion factor $\alpha_{[\text{C II}]}$:** The conversion factor $\alpha_{[\text{C II}]}$ between the [C II] luminosity and the molecular gas mass in our simulated galaxies ranges from $\sim 1 - 200 M_{\odot} L_{\odot}^{-1}$ and does not show a systematic dependence on metallicity in agreement with the findings from Zanella et al. (2018) based on a compilation of galaxies from $z = 0 - 5.5$. Across redshifts, $\alpha_{[\text{C II}]}$ shows a strong correlation with the SFR averaged over 5 Myr and with the SFR change diagnostic $R_{5-200} = \text{SFR}_5 / \text{SFR}_{200}$ (Fig. 8).
- Secondary dependences in the $L_{[\text{C II}]} - M_{\text{mol}}$ relation:** We performed a principal component analysis to quantify sec-

ondary dependences in the [C II]- M_{mol} relation and found a strong dependence on the SFR_5 (the star formation rate measured on a 5 Myr timescale) that evolves with redshift and a weak dependence on metallicity across redshifts (Table 5). The resulting 5-variable PCA relation predicts the true molecular gas within a factor of 1.7 (2.5) at $z = 3$ ($z = 7$). When accounting for typical observational uncertainties on $L_{[\text{C II}]}$, SFR, and gas metallicity, the PCA-based relation predicts the true molecular gas mass within a factor of ~ 2.5 at $3 \leq z \leq 5$.

- What does the [C II] emission really trace?:** We investigated the correlation of $L_{[\text{C II}]}$ with several galaxy-integrated properties, namely the SFR, the molecular gas mass, the total gas mass, and the metal mass in gas phase (M_{metal}). Among these, the [C II] emission in our simulated galaxies shows the tightest correlation with M_{metal} across redshifts.
- Extended [C II] emission:** We observe that our stacked [C II] surface brightness profiles show a similar extent as the low-SFR galaxy sample from Ginolfi et al. (2020), although some individual galaxies also exhibit a similar extent as their high-SFR sample. We further find that galaxies where the [C II] emission extends twice or more farther than the SF activity preferentially exhibit a spatial distribution wherein the bulk ($\gtrsim 70\%$) of the [C II] emission is confined to the central galaxy, while the remaining $\lesssim 30\%$ extends out to larger distances because of the presence of satellites. The typical fractional contribution of satellites to the total [C II]

emission in these galaxies is $\approx 5 - 7$ times higher than that in galaxies without extended emission (see Table 7).

Acknowledgements. The authors thank R. Teyssier for making the RAMSES code publicly available. They gratefully acknowledge the Collaborative Research Center 1601 (SFB 1601 sub-project C5) funded by the Deutsche Forschungsgemeinschaft (DFG, German Research Foundation) – 500700252. Early stages of this work were carried out within the Collaborative Research Centre 956 (SFB 956 sub-project C4), funded by the DFG – 184018867. The authors acknowledge the Gauss Centre for Supercomputing e.V. (www.gauss-centre.eu) for funding this project by providing computing time on the GCS Supercomputer SuperMUC-NG at the Leibniz Supercomputing Centre (<http://www.lrz.de>). They are thankful to the Max Planck Society (MPG) for providing computing time on the supercomputer Raven at the Max Planck Computing and Data Facility (<https://www.mpcdf.mpg.de>), where part of the MARIGOLD simulations were performed. PK is a part of the International Max Planck Research School in Astronomy and Astrophysics, the Bonn Cologne Graduate School, and a guest at the Max Planck Institute for Radio Astronomy in Bonn.

References

- Accurso, G., Saintonge, A., Catinella, B., et al. 2017, *MNRAS*, 470, 4750
- Aravena, M., Heintz, K., Dessauges-Zavadsky, M., et al. 2024, *A&A*, 682, A24
- Asplund, M., Grevesse, N., Sauval, A. J., & Scott, P. 2009, *ARA&A*, 47, 481
- Atek, H., Labbé, I., Furtak, L. J., et al. 2024, *Nature*, 626, 975
- Bernal, J. L. & Kovetz, E. D. 2022, *A&A Rev.*, 30, 5
- Béthermin, M., Fudamoto, Y., Ginolfi, M., et al. 2020, *A&A*, 643, A2
- Bigiel, F., Leroy, A., Walter, F., et al. 2008, *AJ*, 136, 2846
- Bothwell, M. S., Maiolino, R., Cicone, C., Peng, Y., & Wagg, J. 2016, *A&A*, 595, A48
- Bouwens, R. J., Smit, R., Schouws, S., et al. 2022, *ApJ*, 931, 160
- Carniani, S., Maiolino, R., Smit, R., & Amorín, R. 2018, *ApJ*, 854, L7
- Clarke, L., Shapley, A. E., Sanders, R. L., et al. 2024, arXiv e-prints, arXiv:2406.05178
- Cormier, D., Abel, N. P., Hony, S., et al. 2019, *A&A*, 626, A23
- da Cunha, E., Groves, B., Walter, F., et al. 2013, *ApJ*, 766, 13
- Davé, R., Crain, R. A., Stevens, A. R. H., et al. 2020, *MNRAS*, 497, 146
- De Breuck, C., Lundgren, A., Emonts, B., et al. 2022, *A&A*, 658, L2
- De Looze, I., Baes, M., Bendo, G. J., Cortese, L., & Fritz, J. 2011, *MNRAS*, 416, 2712
- De Looze, I., Cormier, D., Lebouteiller, V., et al. 2014, *A&A*, 568, A62
- Dessauges-Zavadsky, M., Ginolfi, M., Pozzi, F., et al. 2020, *A&A*, 643, A5
- D’Eugenio, C., Daddi, E., Liu, D., & Gobat, R. 2023, *A&A*, 678, L9
- Díaz-Santos, T., Armus, L., Charmandaris, V., et al. 2013, *ApJ*, 774, 68
- Ferland, G. J., Peterson, B. M., Horne, K., Welsh, W. F., & Nahar, S. N. 1992, *ApJ*, 387, 95
- Foreman-Mackey, D., Conley, A., Meierjürgen, W., et al. 2013, emcee: The MCMC Hammer, *Astrophysics Source Code Library*, record ascl:1303.002
- Fudamoto, Y., Smit, R., Bowler, R. A. A., et al. 2022, *ApJ*, 934, 144
- Fujimoto, S., Ouchi, M., Ferrara, A., et al. 2019, *ApJ*, 887, 107
- Fujimoto, S., Silverman, J. D., Béthermin, M., et al. 2020, *ApJ*, 900, 1
- García, K., Narayanan, D., Popping, G., et al. 2024, *ApJ*, 974, 197
- Gehrels, N. 1986, *ApJ*, 303, 336
- Ginolfi, M., Jones, G. C., Béthermin, M., et al. 2020, *A&A*, 633, A90
- Goldsmith, P. F., Langer, W. D., Pineda, J. L., & Velusamy, T. 2012, *ApJS*, 203, 13
- Gong, Y., Cooray, A., Silva, M., et al. 2012, *ApJ*, 745, 49
- Graciá-Carpio, J., Sturm, E., Hailey-Dunsheath, S., et al. 2011, *ApJ*, 728, L7
- Gullberg, B., De Breuck, C., Vieira, J. D., et al. 2015, *MNRAS*, 449, 2883
- Hahn, O. & Abel, T. 2011, *MNRAS*, 415, 2101
- Heintz, K. E., Oesch, P. A., Aravena, M., et al. 2022, *ApJ*, 934, L27
- Heintz, K. E., Shapley, A. E., Sanders, R. L., et al. 2023, *A&A*, 678, A30
- Heintz, K. E., Watson, D., Oesch, P. A., Narayanan, D., & Madden, S. C. 2021, *ApJ*, 922, 147
- Herrera-Camus, R., Bolatto, A. D., Wolfire, M. G., et al. 2015, *ApJ*, 800, 1
- Herrera-Camus, R., Förster Schreiber, N., Genzel, R., et al. 2021, *A&A*, 649, A31
- Hu, C.-Y., Sternberg, A., & van Dishoeck, E. F. 2021, *ApJ*, 920, 44
- Hughes, T. M., Ibar, E., Villanueva, V., et al. 2017, *A&A*, 602, A49
- Hunt, L., Magrini, L., Galli, D., et al. 2012, *MNRAS*, 427, 906
- Katz, H., Galligan, T. P., Kimm, T., et al. 2019, *MNRAS*, 487, 5902
- Katz, H., Rosdahl, J., Kimm, T., et al. 2022, *MNRAS*, 510, 5603
- Kennicutt, Robert C., J. 1998, *ApJ*, 498, 541
- Kennicutt, R. C. & Evans, N. J. 2012, *ARA&A*, 50, 531
- Khatri, P., Porciani, C., Romano-Díaz, E., Seifried, D., & Schäbe, A. 2024, *A&A*, 688, A194
- Klypin, A. A., Trujillo-Gomez, S., & Primack, J. 2011, *ApJ*, 740, 102
- Knollmann, S. R. & Knebe, A. 2009, *ApJS*, 182, 608
- Lagache, G., Cousin, M., & Chatzikos, M. 2018, *A&A*, 609, A130
- Lagos, C. d. P., Crain, R. A., Schaye, J., et al. 2015, *MNRAS*, 452, 3815
- Lagos, C. d. P., Theuns, T., Schaye, J., et al. 2016, *MNRAS*, 459, 2632
- Lambert, T. S., Posses, A., Aravena, M., et al. 2023, *MNRAS*, 518, 3183
- Langer, W. D. & Pineda, J. L. 2015, *A&A*, 580, A5
- Lara-López, M. A., Cepa, J., Bongiovanni, A., et al. 2010, *A&A*, 521, L53
- Le Fèvre, O., Béthermin, M., Faisst, A., et al. 2020, *A&A*, 643, A1
- Leroy, A. K., Walter, F., Brinks, E., et al. 2008, *AJ*, 136, 2782
- Leung, T. K. D., Olsen, K. P., Somerville, R. S., et al. 2020, *ApJ*, 905, 102
- Loiacono, F., Decarli, R., Gruppioni, C., et al. 2021, *A&A*, 646, A76
- Lomaeva, M., De Looze, I., Saintonge, A., & Declair, M. 2022, *MNRAS*, 517, 3763
- Lupi, A., Bovino, S., Capelo, P. R., Volonteri, M., & Silk, J. 2018, *MNRAS*, 474, 2884
- Madau, P. & Dickinson, M. 2014, *ARA&A*, 52, 415
- Madden, S. C., Cormier, D., Hony, S., et al. 2020, *A&A*, 643, A141
- Madden, S. C., Rémy-Ruyer, A., Galametz, M., et al. 2013, *PASP*, 125, 600
- Magnelli, B., Boogaard, L., Decarli, R., et al. 2020, *ApJ*, 892, 66
- Malhotra, S., Kaufman, M. J., Hollenbach, D., et al. 2001, *ApJ*, 561, 766
- Mannucci, F., Cresci, G., Maiolino, R., Marconi, A., & Gnerucci, A. 2010, *MNRAS*, 408, 2115
- Matthee, J., Sobral, D., Boogaard, L. A., et al. 2019, *ApJ*, 881, 124
- Muñoz-Elgueta, N., Arrigoni Battaia, F., Kauffmann, G., et al. 2024, arXiv e-prints, arXiv:2407.17359
- Nelson, R. P. & Langer, W. D. 1999, *ApJ*, 524, 923, (NL99)
- Olsen, K., Greve, T. R., Narayanan, D., et al. 2017, *ApJ*, 846, 105
- Olsen, K. P., Greve, T. R., Brinch, C., et al. 2016, *MNRAS*, 457, 3306
- Olsen, K. P., Greve, T. R., Narayanan, D., et al. 2015, *ApJ*, 814, 76
- Pallottini, A., Ferrara, A., Gallerani, S., Salvadori, S., & D’Odorico, V. 2014, *MNRAS*, 440, 2498
- Pallottini, A., Ferrara, A., Gallerani, S., et al. 2017, *MNRAS*, 465, 2540
- Pineda, J. L., Langer, W. D., & Goldsmith, P. F. 2014, *A&A*, 570, A121
- Planck Collaboration VI. 2020, *A&A*, 641, A6
- Popping, G., Behroozi, P. S., & Peebles, M. S. 2015, *MNRAS*, 449, 477
- Popping, G., Narayanan, D., Somerville, R. S., Faisst, A. L., & Krumholz, M. R. 2019, *MNRAS*, 482, 4906
- Popping, G., van Kampen, E., Decarli, R., et al. 2016, *MNRAS*, 461, 93
- Posses, A., Aravena, M., González-López, J., et al. 2024, arXiv e-prints, arXiv:2403.03379
- Prada, F., Klypin, A. A., Cuesta, A. J., Betancort-Rijo, J. E., & Primack, J. 2012, *MNRAS*, 423, 3018
- Riechers, D. A., Pavesi, R., Sharon, C. E., et al. 2019, *ApJ*, 872, 7
- Rowland, L. E., Hodge, J., Bouwens, R., et al. 2024, *MNRAS*[arXiv:2405.06025]
- Roy, A. & Lapi, A. 2024, arXiv e-prints, arXiv:2407.19007
- Sanders, R. L., Shapley, A. E., Kriek, M., et al. 2015, *ApJ*, 799, 138
- Schaerer, D., Ginolfi, M., Béthermin, M., et al. 2020, *A&A*, 643, A3
- Scoville, N., Lee, N., Vanden Bout, P., et al. 2017, *ApJ*, 837, 150
- Somerville, R. S., Lee, K., Ferguson, H. C., et al. 2004, *ApJ*, 600, L171
- Spiegelhalter, D. J., Best, N. G., Carlin, B. P., & Van Der Linde, A. 2002, *Journal of the Royal Statistical Society Series B: Statistical Methodology*, 64, 583
- Springel, V., Wang, J., Vogelsberger, M., et al. 2008, *MNRAS*, 391, 1685
- Stacey, G. J., Hailey-Dunsheath, S., Ferkinhoff, C., et al. 2010, *ApJ*, 724, 957
- Swinbank, A. M., Karim, A., Smail, I., et al. 2012, *MNRAS*, 427, 1066
- Szomoru, D., Franx, M., van Dokkum, P. G., et al. 2013, *ApJ*, 763, 73
- Tajiri, Y. & Umemura, M. 1998, *ApJ*, 502, 59
- Teyssier, R. 2002, *A&A*, 385, 337
- Tremonti, C. A., Heckman, T. M., Kauffmann, G., et al. 2004, *ApJ*, 613, 898
- Trenti, M. & Stiavelli, M. 2008, *ApJ*, 676, 767
- Vallini, L., Gallerani, S., Ferrara, A., Pallottini, A., & Yue, B. 2015, *ApJ*, 813, 36
- Vizgan, D., Greve, T. R., Olsen, K. P., et al. 2022, *ApJ*, 929, 92
- Walter, F., Carilli, C., Neeleman, M., et al. 2020, *ApJ*, 902, 111
- Wolfire, M. G., Hollenbach, D., & McKee, C. F. 2010, *ApJ*, 716, 1191
- Yan, L., Sajina, A., Loiacono, F., et al. 2020, *ApJ*, 905, 147
- Yang, X., Mo, H. J., & van den Bosch, F. C. 2003, *MNRAS*, 339, 1057
- Zanella, A., Daddi, E., Magdis, G., et al. 2018, *MNRAS*, 481, 1976

Appendix A: Modelling [C II] emission

For a two-level system such as the C^+ fine-structure transition, the excitation temperature (T_{ex}) captures the relative population in the upper (u) and lower (l) energy levels of the transition:

$$\frac{n_u}{n_l} = \frac{g_u}{g_l} e^{-T_s/T_{\text{ex}}}. \quad (\text{A.1})$$

Here g_u and g_l are the statistical weights of the upper and lower levels with an energy difference of $k_B T_s$ (k_B being the Boltzmann constant), and $n_u + n_l = n_{C^+}$. In statistical equilibrium, level populations are determined by the balance between excitation and deexcitation processes:

$$n_l(B_{lu}U + C_{lu}) = n_u(A_{ul} + B_{ul}U + C_{ul}), \quad (\text{A.2})$$

where U is the energy density at the transition frequency ν ; A_{ul} , B_{ul} and B_{lu} are the Einstein coefficients for spontaneous decay, stimulated decay, and stimulated excitation, respectively, C_{ul} and C_{lu} are the collision deexcitation and excitation rates and, in the case of multiple collision partners, can be obtained from the respective collision rate coefficients and number densities as:

$$C_{ul} = \sum_{i=1}^N R_{ul,i} n_i. \quad (\text{A.3})$$

The upward and downward collision rate coefficients are related as:

$$R_{lu} = R_{ul} \frac{g_u}{g_l} e^{-T_s/T_{\text{kin}}}, \quad (\text{A.4})$$

where T_{kin} is the kinetic temperature related to the thermal motions of the collision partner. The collision rate coefficients are taken from [Goldsmith et al. \(2012\)](#):

$$R_{ul}(e^-) = 8.7 \times 10^{-8} (T_e/2000)^{-0.37} \text{ cm}^3 \text{ s}^{-1}, \quad (\text{A.5})$$

$$R_{ul}(\text{H}) = 7.6 \times 10^{-10} (T_{\text{kin}}/100)^{0.14} \text{ cm}^3 \text{ s}^{-1}, \quad (\text{A.6})$$

$$R_{ul}(\text{H}_2) = 3.8 \times 10^{-10} (T_{\text{kin}}/100)^{0.14} \text{ cm}^3 \text{ s}^{-1}, \quad (\text{A.7})$$

where T_e is the electron temperature. In the following, we assume $T_e = T_{\text{kin}}$. We obtain the kinetic temperature at each sub-grid density using the temperature density relation (from [Hu et al. 2021](#)) and is identical to the one adopted in HYACINTH (see [Khatri et al. 2024](#), for details). The C^+ and H_2 number densities are obtained directly from the simulations. To obtain the number density of atomic hydrogen (H), we assume that gas at densities $n_{\text{H,tot}} \gtrsim 0.013 \text{ cm}^{-3}$ is well-shielded and $n_{\text{H}^+} = 0$ ([Tajiri & Umemura 1998](#)); below these densities, we assume all hydrogen to be ionised, i.e., $n_{\text{H}^+} = n_{\text{H,tot}}$. The electron number density follows from charge conservation i.e., $n_{e^-} = n_{C^+} + n_{\text{H}^+}$. Note that, similar to [Gong et al. \(2012\)](#) and [Vallini et al. \(2015\)](#), we do not consider the pumping effect from the soft UV background from stars at 1330 Å.

Now, suppose that a given grid cell of sidelength L can be split into N plane-parallel slices as shown in Fig. A.1. In the following, we take $N = 3$ for simplicity, but in practice, use 20 slices in each slice, which were sufficient to reach convergence. The width and density of each slice are determined by the sub-grid density PDF (same as in HYACINTH) within the cell. If $T_{\text{ex},i}$ is the excitation temperature in slice i , then the energy density generated in the slice at the transition frequency ν can then be written as

$$U_\nu(T_{\text{ex},i}) = \frac{4\pi}{c} B_\nu(T_{\text{ex},i}) = \frac{8\pi h \nu^3}{c^3} \frac{1}{\exp(h\nu/k_B T_{\text{ex},i}) - 1}.$$

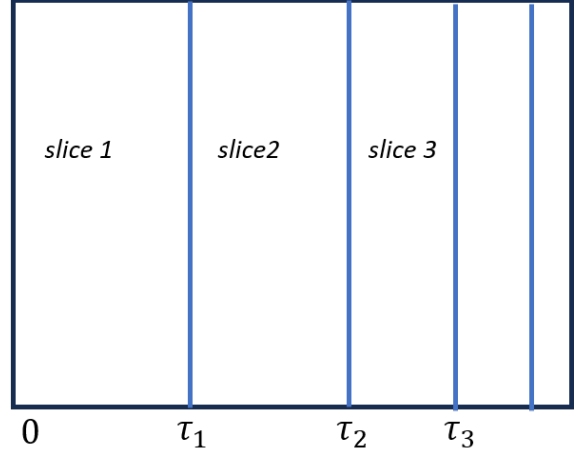


Fig. A.1: A schematic of the plane-parallel slices in a grid cell. (A.8)

Assuming the entire region is permeated by a background like the CMB at temperature T_{bg} with energy density $U_\nu(T_{\text{bg}})$, the total energy density in a slice will have three contributions:

1. the energy density generated in the slice weighted by the fraction of the energy that does not escape the slice (self-absorption, denoted by κ_{ii});
2. the energy density from all other slices where the energy density of the emitting slice i is weighted by the fraction that is absorbed by the absorbing slice j (denoted by κ_{ij});
3. the energy density from the background (CMB in this case).

Following [Goldsmith et al. \(2012\)](#), the total energy density in the slice at the [C II] frequency can be written as:

$$U_1 = (1 - \kappa_{11}) U_\nu(T_{\text{bg}}) + \kappa_{11} U_\nu(T_{\text{ex},1}) + \kappa_{21} U_\nu(T_{\text{ex},2}) + \kappa_{31} U_\nu(T_{\text{ex},3}). \quad (\text{A.9})$$

Similarly,

$$U_2 = (1 - \kappa_{22}) U_\nu(T_{\text{bg}}) + \kappa_{12} U_\nu(T_{\text{ex},1}) + \kappa_{22} U_\nu(T_{\text{ex},2}) + \kappa_{32} U_\nu(T_{\text{ex},3}); \quad (\text{A.10})$$

and

$$U_3 = (1 - \kappa_{33}) U_\nu(T_{\text{bg}}) + \kappa_{13} U_\nu(T_{\text{ex},1}) + \kappa_{23} U_\nu(T_{\text{ex},2}) + \kappa_{33} U_\nu(T_{\text{ex},3}). \quad (\text{A.11})$$

If U_1, U_2, U_3 are known, they can be used to evaluate the level population in each slice by balancing the upward and downward transitions as (e.g., for slice 1):

$$n_{u,1} (A_{ul} + B_{ul}U_1 + C_{ul}) = n_{l,1} (B_{lu}U_1 + C_{lu}), \quad (\text{A.12})$$

and the excitation temperature $T_{\text{ex},1}$ can be obtained using Eq. (A.1). Following [Goldsmith et al. \(2012\)](#), the optical depth for slice 1 can be calculated from the excitation temperature $T_{\text{ex},1}$ as:

$$\begin{aligned} \tau_1 &= \frac{h B_{lu} N(C^+)}{\delta \nu} \frac{1 - e^{-h\nu/k_B T_{\text{ex},1}}}{1 + (g_u/g_l) e^{-h\nu/k_B T_{\text{ex},1}}} \\ &= \frac{g_u}{g_l} \frac{A_{ul} \lambda_{ul}^3 N(C^+)}{8\pi \sqrt{8 \ln(2)} \sigma_\nu} \frac{1 - e^{-h\nu/k_B T_{\text{ex},1}}}{1 + (g_u/g_l) e^{-h\nu/k_B T_{\text{ex},1}}}, \end{aligned} \quad (\text{A.13})$$

where λ_{ul} is the wavelength of the [C II] line and $N(\text{C}^+)$ denotes the column density of C^+ from the edge of the cell to the slice i . The above expression approximates the line profile function ϕ_ν at line center by δv^{-1} , where δv is the line width ($\delta v = \sqrt{8 \ln 2} \sigma_v$ for a Gaussian velocity distribution with 1-D velocity dispersion σ_v). We obtain the 1-D velocity dispersion σ_v for the cells in our simulations following the approach of Olsen et al. (2015): the velocity dispersion in a giant molecular cloud (GMC) of mass M_{GMC} and radius R_{GMC} is given as

$$\sigma_v = 1.2 \text{ km s}^{-1} \left(\frac{R_{\text{GMC}}}{\text{pc}} \right)^{-1/2} \left(\frac{M_{\text{GMC}}}{290 M_\odot} \right)^{1/2}, \quad (\text{A.14})$$

where we approximate $R_{\text{GMC}} \approx \frac{1}{2} \Delta L$ and $M_{\text{GMC}} = M_{\text{gas, cell}}$.

The system of equations (A.1), (A.9)-(A.13) can be solved iteratively. We start with the optically thin case where all emitted radiation freely escapes (i.e., $\kappa_{ij} = 0 \forall \{i, j\}$), and obtain an initial estimate of $n_{u,i}$ using Eq. (A.12). These estimates are then used to obtain a first estimate of $T_{\text{ex},1}, T_{\text{ex},2}, T_{\text{ex},3}$ using Eq. (A.1). These determine the optical depths τ_1, τ_2, τ_3 using Eq. (A.13). Using these, the κ values can be updated and the entire procedure is repeated until convergence⁹.

Once we have a set of self-consistent T_{ex} and κ values, we can calculate the emissivity of each slice. Following Goldsmith et al. (2012), the emissivity in slice 1 can be written as

$$\epsilon_1 = n_{u,1} A_{ul} \gamma_1 h \nu \left[1 - \frac{e^{(h\nu/k_B T_{\text{ex},1})} - 1}{e^{(h\nu/k_B T_{\text{bg}})} - 1} \right], \quad (\text{A.15})$$

where

$$\gamma_i = 1.0 - \sum_{j=1}^3 \kappa_{ij} \quad (\text{A.16})$$

denotes the final escape fraction for slice i , i.e., the fraction of photons emitted in slice i that manage to escape the cell and accounts for absorption from all intervening slices.

The total luminosity from the cell can be written as:

$$L_{[\text{C II}]} = \sum_{i=1}^N \gamma_i \epsilon_i \Delta V_i, \quad (\text{A.17})$$

where $\Delta V_i = \mathcal{P}_V(n_i) \Delta n_i V_{\text{cell}}$ is the volume of each slice, and N is the number of slices in the cell. The galaxy luminosity is obtained by summing over the [C II] emission from all cells within the galaxy. We note that our method assumes that the [C II] emission from the different grid cells are radiatively decoupled and the total [C II] emission from a galaxy is the sum of the emission from each cell.

Appendix B: Model Validation

We validate our [C II] emission model by comparing its output with the photoionization code CLOUDY (version 17.02; Ferland et al. 1992). To do this, we compute the luminosity emerging from a plane-parallel slab with a side length of $\Delta x = 38 \text{ pc}$, corresponding to the minimum spatial resolution achieved in our M25 run at $z = 4$. The CMB is included for $z = 4$.

To span the range of gas densities and metallicities exhibited by PDRs and molecular clouds, we compute the luminosity for a 2D grid with hydrogen number density $n_{\text{H}} \in [10^0, 10^4] \text{ cm}^{-3}$

⁹ Here convergence is defined as the point when the difference between the norm of κ matrices of successive iterations is $\leq 10^{-4}$.

and gas metallicity $Z_{\text{gas}} \in [10^{-1.8}, 10^0] Z_\odot$. The slabs have a uniform density, metallicity and temperature. We assume that the kinetic temperature is uniform throughout the slab. For each set of $(n_{\text{H}}, Z_{\text{gas}})$ values, we obtain the temperature using the metallicity-dependent temperature density relation from Hu et al. (2021, same as in HYACINTH). We assume that the elemental abundance of carbon $f_{\text{C,tot}}$ scales as $f_{\text{C,tot}} = 2.9 \times 10^{-4} Z_{\text{gas}}/Z_\odot$ (Asplund et al. 2009). For each of these models, CLOUDY computes the abundances of different chemical species as a function of the depth into the slab. The C^+ , H_2 , and H I abundances are used as inputs to our model compute the emergent luminosity from the model cells. We further assume $n_{e^-} = n_{\text{C}^+}$.

The results of the comparison are shown in Fig. B.1. In the following, we denote the [C II] luminosity predicted by our model as L and the one from CLOUDY as L_{CLOUDY} . At all values of T_{kin} , the distribution of L is very similar to L_{CLOUDY} , with L from both approaches increasing with density at a fixed metallicity. Conversely, at fixed densities $n_{\text{H}} \lesssim 10^3 \text{ cm}^{-3}$, L increases with metallicity and the variation with metallicity is minimal at higher densities. At $\log(Z_{\text{gas}}/Z_\odot) \gtrsim 10^{-0.6}$ (i.e., $Z_{\text{gas}} \gtrsim 0.25 Z_\odot$), our model overpredicts $L_{[\text{C II}]}$ at low densities ($n_{\text{H}} \lesssim 10^2 \text{ cm}^{-3}$) and underpredicts at intermediate densities ($10^2 \text{ cm}^{-3} \lesssim n_{\text{H}} \lesssim 10^3 \text{ cm}^{-3}$). In most of the parameter space there is a $\leq 30\%$ deviation between the $L_{[\text{C II}]}$ from the two approaches, particularly at high densities ($n_{\text{H}} \gtrsim 10^3 \text{ cm}^{-3}$).

Appendix C: Fit to the simulated luminosity function

Fig. C.1 shows a comparison between the Schechter function and double power-law fits to the predicted [C II] LFs from our simulations at $3 \leq z \leq 7$.

In Fig. C.2, we show the covariance distributions obtained from the Markov Chain Monte Carlo (MCMC) fitting of our predicted [C II] luminosity function at $z = 4$ with a DPL given in Eq. 2. The fitting was performed using the python package emcee and includes two parameters – Δ_{M25} and Δ_{M50} that represent variation of the $\log \phi$ of the two simulation volumes from the cosmic $\log \phi^*$, because of sample variance. We see that the posterior distributions of the all parameters are well-behaved and smooth, and that the three parameters are highly correlated. We obtain similar results at other redshifts.

Appendix D: Surface densities

In Fig. D.1, we show a scatter plot of the surface densities of CO and C^+ as a function of the SFR (left), gas (middle), and metal (right) surface density. In all panels, we find that while Σ_{CO} continues to increase at high surface densities, Σ_{C^+} shows a plateau. This results in a decrease in the slope of the $\log \Sigma_{[\text{C II}]}$ versus $\log \Sigma_{\text{SFR}}$ curve at high Σ_{SFR} .

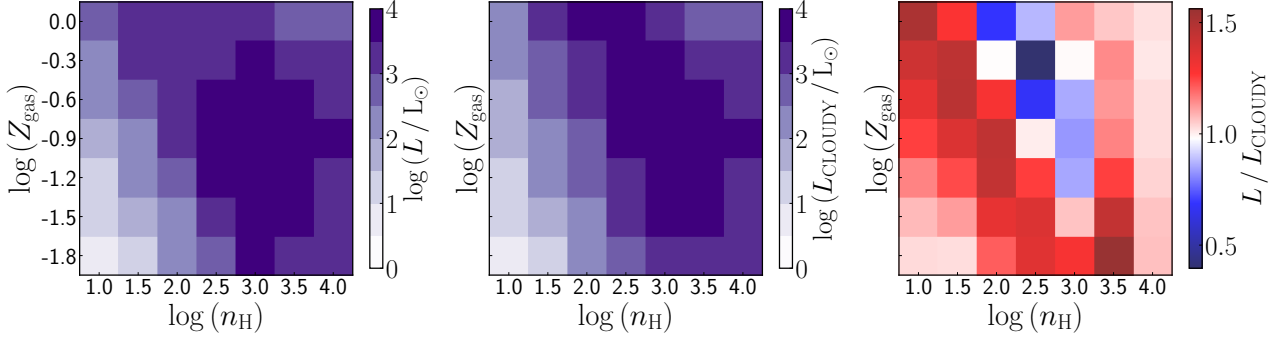


Fig. B.1: Tests of [C II] emission model with CLOUDY. The left and middle panels show, respectively, the luminosity from our model and CLOUDY, while the right panel shows the ratio of the two. For each set of $(n_{\text{H}}, Z_{\text{gas}})$ values, the temperature is obtained using the temperature-density relation from Hu et al. (2021).

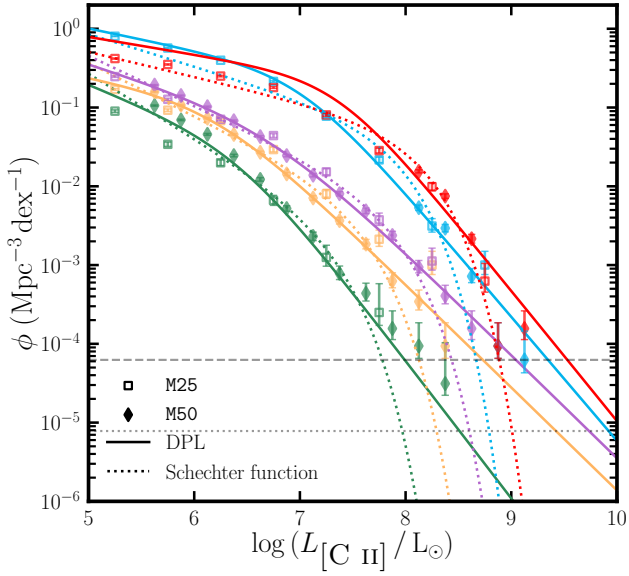


Fig. C.1: Comparison of the Schechter function (dotted lines) and DPL (solid lines) fits to our simulated LFs from the two simulations at different redshifts (from top to bottom, z increases from 3 to 7). The open squares and diamonds represent the separate LFs from the simulations that are used to obtain the fit parameters using an MCMC analysis. The error bars represent the 16 CL upper and lower Poisson uncertainties on number counts (Gehrels 1986). The dashed and dotted horizontal lines represent a number count of 1 per dex in the entire simulation volume of M25 and M50, respectively.

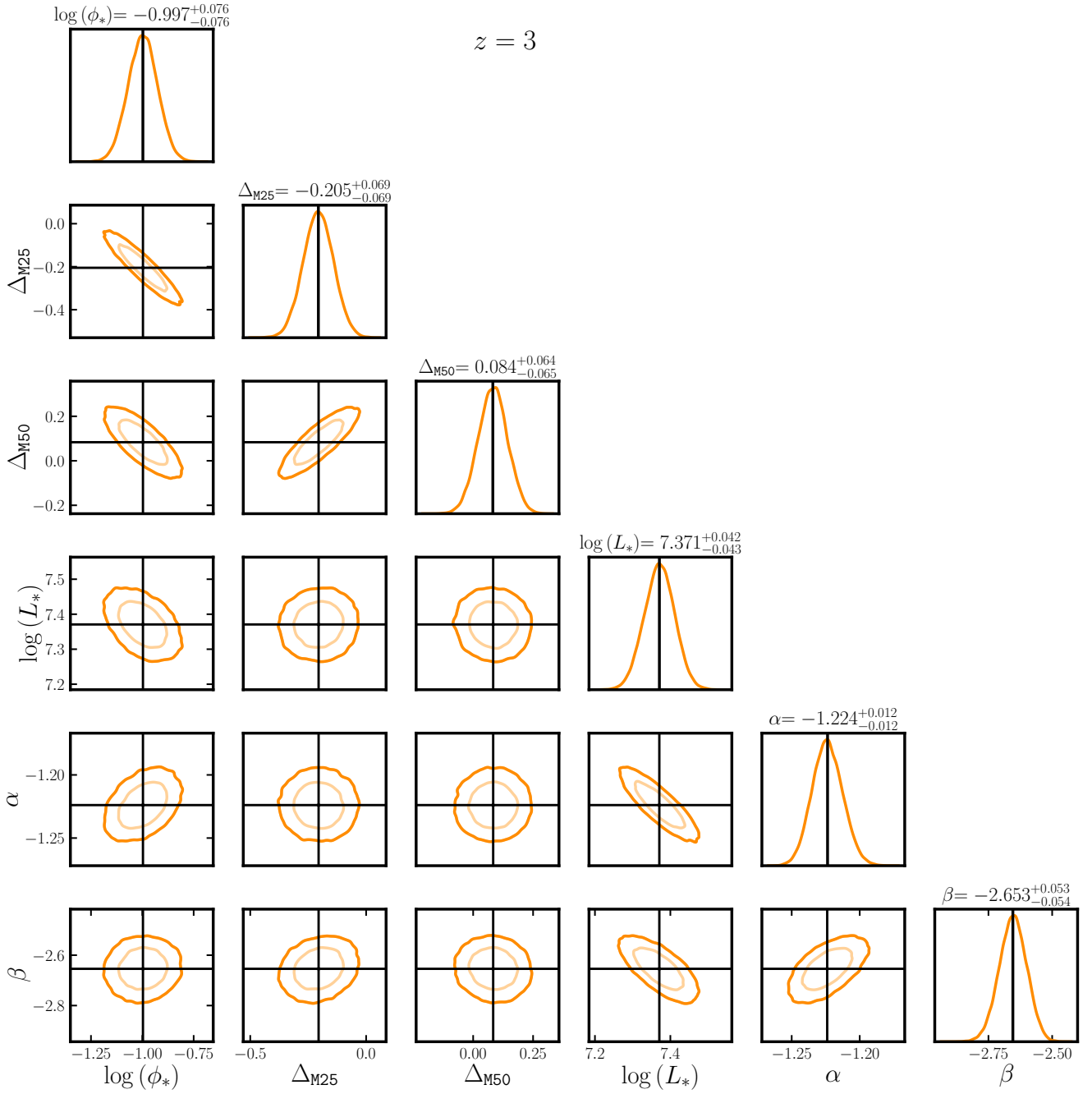


Fig. C.2: Covariance distributions and PDFs of the double power-law function (Eq. 2) parameters: ϕ_* , L_* , α , β , and two additional parameters: Δ_{M25} and Δ_{M50} , from MCMC runs using the python package `emcee` for simulated LF at $z = 3$.

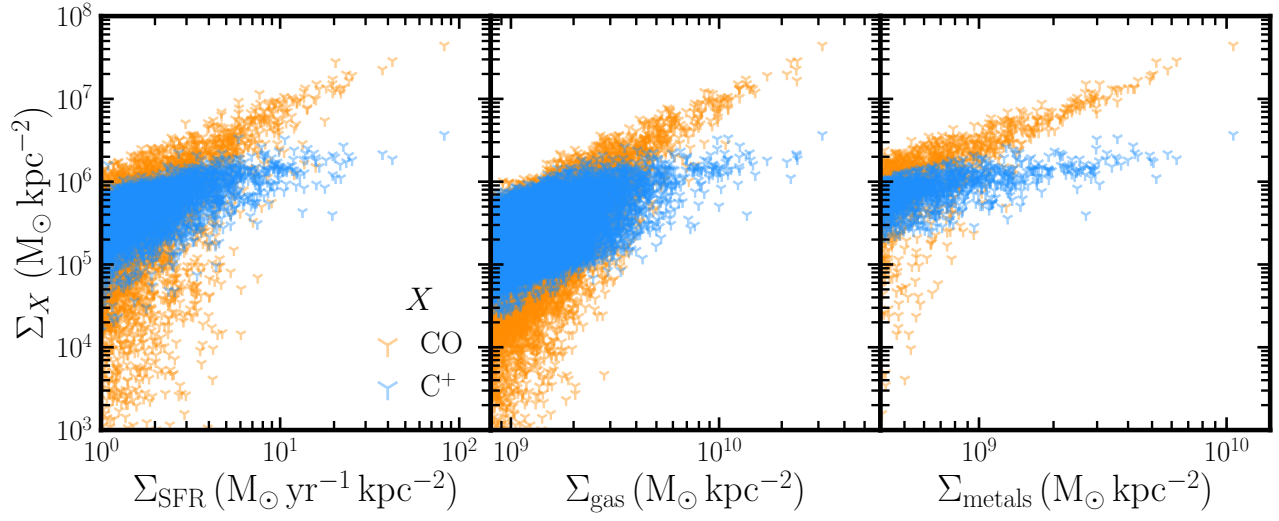


Fig. D.1: The surface density of CO and C⁺ as a function of the SFR surface density (left), the total gas surface density (middle), and the total metal surface density (right), for galaxies used in Fig. 6.